BLOC-2 targets recycling endosomal tubules to melanosomes for cargo delivery

Megan K. Dennis,[1,2,3*] Adriana R. Mantegazza,[1,2,3*] Olivia L. Snir,[2,3] Danièle Tenza,[5,6] Amanda Acosta-Ruiz,[1,2,3] Cédric Delevoye,[5,6] Richard Zorger,[4] Anand Sitaram,[2,3] Wilfredo de Jesus-Rojas,[2,3] Keerthana Ravichandran,[8] John Rux,[2,9] Elena V. Sviderskaya,[10] Dorothy C. Bennett,[10] Graça Raposo,[5,6,7] Michael S. Marks,[1,2,3**] and Subba Rao Gangi Setty[2,8**]

[1]Department of Pathology and Laboratory Medicine, Children's Hospital of Philadelphia, Philadelphia, PA 19104
[2]Department of Pathology and Laboratory Medicine, [3]Department of Physiology, and [4]Penn Vision Research Center, University of Pennsylvania, Philadelphia, PA 19104
[5]Institut Curie, Centre de Recherche; [6]Structure and Membrane Compartments, Centre National de la Recherche Scientifique, Unité Mixte de Recherche (UMR) 144; and [7]Cell and Tissue Imaging Facility, Centre National de la Recherche Scientifique UMR144, Paris F-75248, France
[8]Department of Microbiology and Cell Biology, Indian Institute of Science, Bangalore, India 560 012
[9]In Silico Molecular, LLC, Blue Bell, PA 19422
[10]Molecular Cell Sciences Research Centre, St. George's, University of London, London SW17 0RE, England, UK

Hermansky–Pudlak syndrome (HPS) is a group of disorders characterized by the malformation of lysosome-related organelles, such as pigment cell melanosomes. Three of nine characterized HPS subtypes result from mutations in subunits of BLOC-2, a protein complex with no known molecular function. In this paper, we exploit melanocytes from mouse HPS models to place BLOC-2 within a cargo transport pathway from recycling endosomal domains to maturing melanosomes. In BLOC-2–deficient melanocytes, the melanosomal protein TYRP1 was largely depleted from pigment granules and underwent accelerated recycling from endosomes to the plasma membrane and to the Golgi. By live-cell imaging, recycling endosomal tubules of wild-type melanocytes made frequent and prolonged contacts with maturing melanosomes; in contrast, tubules from BLOC-2–deficient cells were shorter in length and made fewer, more transient contacts with melanosomes. These results support a model in which BLOC-2 functions to direct recycling endosomal tubular transport intermediates to maturing melanosomes and thereby promote cargo delivery and optimal pigmentation.

Introduction

Lysosome-related organelles (LROs) comprise a class of cell type–specific subcellular membranous compartments that derive from the endocytic pathway but fulfill diverse physiological functions (Dell'Angelica et al., 2000; Raposo et al., 2007; Marks et al., 2013). Although some LROs are modified lysosomes, others—such as pigment cell melanosomes and platelet dense granules—are discrete structures that coexist with endolysosomes and are thus generated within their host cells by specialized pathways (Raposo et al., 2007; Sitaram and Marks, 2012; Marks et al., 2013). Defects in such pathways underlie heritable diseases such as Hermansky–Pudlak syndrome (HPS), characterized by oculocutaneous albinism, excessive bleeding, and various other symptoms as a result of malformation of melanosomes, dense granules, and other LROs, respectively (Huizing et al., 2008; Wei and Li, 2013). The affected genes in the nine known forms of HPS encode subunits of four protein complexes—adaptor protein-3 (AP-3) and biogenesis of LROs complex (BLOC)-1, -2, and -3 (Dell'Angelica, 2004; Marks et al., 2013; Wei and Li, 2013). How these complexes function in LRO biogenesis is only partially known.

*M.K. Dennis and A.R. Mantegazza contributed equally to this paper.

**M.S. Marks and S.R.G. Setty contributed equally to this paper.

Correspondence to Michael S. Marks: marksm@mail.med.upenn.edu

Abbreviations used in this paper: AF488, Alexa Fluor 488; AP-3, adaptor protein-3; BFA, brefeldin A; BLOC, biogenesis of lysosome-related organelles complex; CHX, cycloheximide; CMV, cytomegalovirus; CTxB, cholera toxin B subunit; DOPA, 3,4-dihydroxyphenylalanine; fps, frame per second; HPS, Hermansky–Pudlak syndrome; IFM, immunofluorescence microscopy; LRO, lysosome-related organelle; mCh, mCherry; MMLV, Maloney murine leukemia virus; MuHA, Muted-HA; OCA2, oculocutaneous albinism 2; STX13, syntaxin-13; TfR, transferrin receptor; TYR, tyrosinase; TYRP1, TYR-related protein-1; WT, wild type.

The Rockefeller University Press $30.00
J. Cell Biol. Vol. 209 No. 4 563–577
www.jcb.org/cgi/doi/10.1083/jcb.201410026

The least understood HPS-associated complex is BLOC-2, comprised of subunits mutated in HPS types 3, 5, and 6 and their mouse models (Di Pietro et al., 2004; Gautam et al., 2004). BLOC-2 likely plays a regulatory role in LRO biogenesis, as BLOC-2–deficient HPS patients lack the lung pathology observed in BLOC-3– and AP-3–deficient patients (Huizing et al., 2009), and BLOC-2–deficient mice have less severe pigmentary and platelet aggregation defects than other HPS models (Novak et al., 1984, 1988; Zhang et al., 2003; Gautam et al., 2004). BLOC-2 subunits are conserved throughout vertebrate evolution (Daly et al., 2013) and in *Drosophila melanogaster* (Cheli and Dell'Angelica, 2010) but lack obvious structural features except for WD40 domains in HPS5 (Zhang et al., 2003) and a potential clathrin binding domain in HPS3 (Helip-Wooley et al., 2005). BLOC-2 associates with other components required for LRO biogenesis, including the cell-restricted Rab GTPases RAB32 and RAB38 (Bultema et al., 2012) and a cohort of BLOC-1 (Di Pietro et al., 2006; Salazar et al., 2006, 2009), and HPS6 was reported to regulate lysosomal positioning and maturation in HeLa cells (Li et al., 2014). However, a detailed understanding of how BLOC-2 influences protein delivery to LROs is lacking.

Melanosomes in epidermal melanocytes provide an excellent model to dissect HPS-associated complex function in LRO biogenesis (Raposo and Marks, 2007; Sitaram and Marks, 2012). Nonpigmented stage I and II melanosome precursors segregate from vacuolar early endosomes (Raposo et al., 2001) and mature into stage III and IV pigmented granules by delivery of melanogenic integral membrane enzymes and transporters via tubulovesicular carriers. Melanosome cargo is delivered from distinct early endosomal domains via at least two pathways. The enzyme tyrosinase (TYR) is primarily delivered to melanosomes by a pathway that requires AP-3 but not BLOC-1 (Huizing et al., 2001; Theos et al., 2005; Setty et al., 2007, 2008). Other melanosome cargoes, such as TYR-related protein-1 (TYRP1) and oculocutaneous albinism type 2 (OCA2), and a smaller cohort of TYR, exploit a distinct pathway that requires BLOC-1 for cargo exit from vacuolar early endosomes (Setty et al., 2007, 2008; Sitaram et al., 2012). Melanosomal delivery by this pathway employs tubular recycling endosomal transport intermediates that require the adaptor AP-1 and the microtubule motor KIF13A for their formation (Delevoye et al., 2009). Other known effectors of melanosomal transport such as RAB32, RAB38, and their exchange factor, BLOC-3, likely also function in this pathway, as they are required for melanosome localization of a similar set of cargoes in some melanocytic cells (Di Pietro et al., 2006; Wasmeier et al., 2006; Bultema et al., 2012; Gerondopoulos et al., 2012). Although TYRP1 and TYR distributions are altered in BLOC-2–deficient cells (Richmond et al., 2005; Helip-Wooley et al., 2007; Setty et al., 2007) and BLOC-2 localizes to transferrin-accessible endosomal tubules with characteristics of the KIF13A-dependent transport intermediates (Di Pietro et al., 2006), it is not known at which step BLOC-2 functions in melanosome cargo transport.

Here, we use immortalized melanocytes from mouse HPS models, quantitative analyses of melanosome cargo localization and trafficking, and live-cell imaging of transport intermediates to place BLOC-2 function at a late stage of cargo delivery in the BLOC-1–dependent transport pathway. Our data show that BLOC-2 directs the tubular transport intermediates to interact specifically with maturing melanosomes either by "tethering" or by stabilizing the transport intermediates.

Results

Hypopigmentation in BLOC-2–deficient melanocytes and rescue by missing subunit expression

To identify the cargo transport pathway in which BLOC-2 functions, we first sought to define how loss of BLOC-2 expression influences melanosome cargo distribution and dynamics. We exploited immortalized melan-coa melanocytes (heretofore referred to as BLOC-2^{-}; Suzuki et al., 2001) derived from C57BL/6-*Hps3*$^{coa/coa}$ (*cocoa*) mice in which an inactivating mutation in *Hps3* concomitantly destabilizes HPS5 and HPS6 (Gautam et al., 2004). By bright-field microscopy, BLOC-2^{-} cells were hypopigmented relative to wild-type (WT) C57BL/6-derived melan-Ink4a melanocytes (Sviderskaya et al., 2002) but heterogeneous; some cells (~20%) harbored many lightly pigmented granules throughout the cytoplasm, most cells (~70%) contained few scattered granules (Fig. 1 *a*), and some (~10% at early passages) lacked pigment granules altogether. The relative fraction of each pigmentation type varied with culture conditions. Similarly, heterogeneous but low levels of pigmentation were observed in immortalized melan-ru (Fig. S1 *d*) and melan-ru2 melanocytes (not depicted) derived from BLOC-2–deficient *ruby eye* (*Hps6*^{ru}) and *ruby eye 2* (*Hps5*^{ru2}) mice. Pigmentation and HPS6 expression in BLOC-2^{-} cells were restored to WT levels by stable expression of human HPS3 (melan-coa:hHPS3 or BLOC-2^{R}), but not of the HA-tagged irrelevant BLOC-1 subunit, Muted-HA (MuHA; melan-coa:MuHA or BLOC-2^{-C} for negative control; Fig. 1, *b–d*). Electron microscopy analysis showed that compared with "rescued" BLOC-2^{R}, BLOC-2^{-} cells harbored fewer fully pigmented stage IV melanosomes that were unusually rounded, and more striated nonpigmented stage II and partially pigmented stage III melanosomes with irregular melanin deposits (Fig. 1, *e* and *f*), consistent with published results (Suzuki et al., 2001). These data show that melanosome maturation beyond stage II is impaired in the absence of BLOC-2. Except where indicated, the remaining experiments compare nonclonal populations of BLOC-2^{-} and/or BLOC-2^{-C} cells to BLOC-2^{R} or WT melanocytes.

Melanosomal proteins are partially mislocalized to endosomes and the Golgi in BLOC-2–deficient melanocytes

In BLOC-1–deficient (BLOC-1^{-}) melanocytes or human melanoma cells depleted of KIF13A or AP-1, melanosomal cargoes such as TYRP1 accumulate in enlarged early endosomes as a result of failed extraction from endosomes toward melanosomes and consequent increased endosomal recycling (Setty et al., 2007; Delevoye et al., 2009). To define cargo mislocalization in BLOC-2–deficient melanocytes, we first used deconvolution immunofluorescence microscopy (IFM) to assess localization of TYRP1 relative to early sorting and recycling endosomes

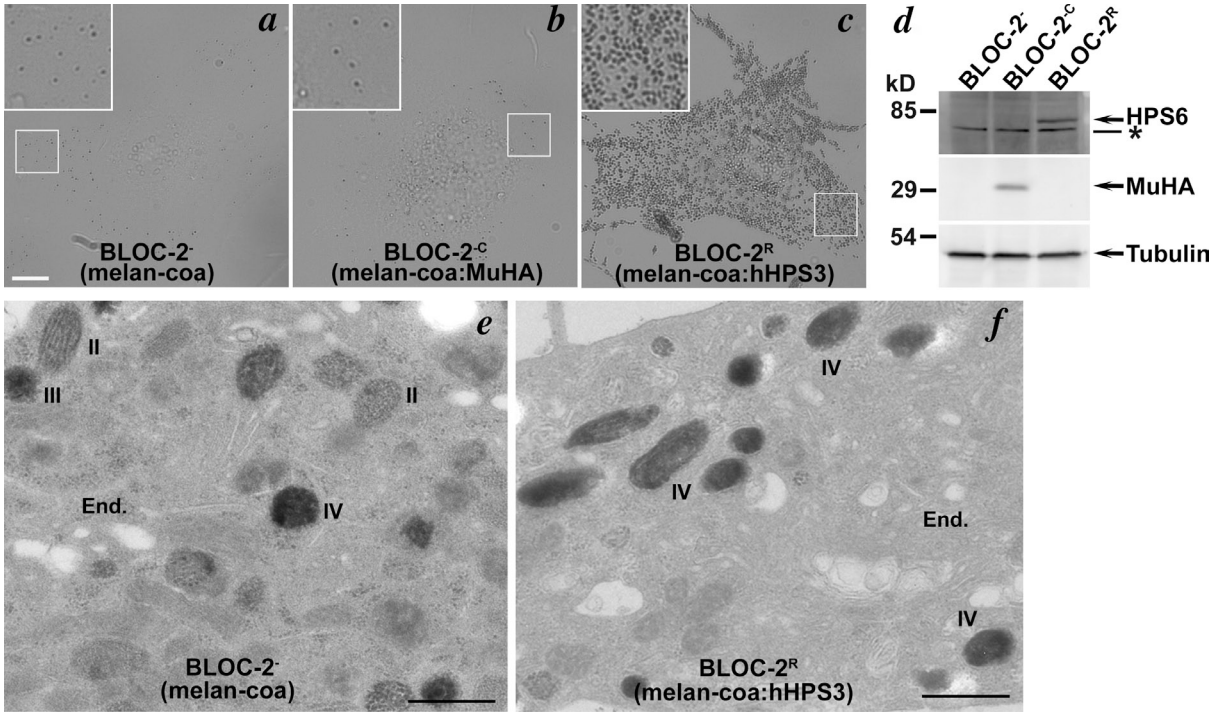

Figure 1. **BLOC-2$^-$ melanocytes are hypopigmented and pigmentation is restored by expression of the deficient BLOC-2 subunit.** (*a–c*) Bright-field microscopy analysis of untransfected HPS3-deficient melan-coa (BLOC-2$^-$, *a*) or stable transfectants expressing Muted-HA (melan-coa:MuHA or BLOC-2^{-C}, *b*) or hHPS3 (melan-coa:hHPS3 or BLOC-2^R, *c*). Images were taken at identical lighting and camera settings. Insets, 2.5× magnification of boxed regions. Bar, 10 µm. (*d*) BLOC-2$^-$, BLOC-2^{-C}, and BLOC-2^R whole cell lysates were fractionated by SDS-PAGE and immunoblotted with antibodies to HPS6, HA epitope, or γ-tubulin as a loading control. (left) Migration of molecular mass markers (in kilodaltons); arrows indicate relevant bands; the asterisk shows a nonspecific band recognized by anti-HPS6 antiserum. (*e* and *f*) Standard electron microscopy analysis of BLOC-2$^-$ and BLOC-2^R melanocytes. End., endosomes; II, III, and IV, different stages of melanosomes. Bars, 500 nm.

marked by syntaxin-13 (STX13). STX13 distribution was generally similar in BLOC-2$^-$ and BLOC-2^R cells (Fig. 2 and Fig. S1, *a–d*). Compared with BLOC-2^R cells, in which only 14 ± 7% of peripheral TYRP1-positive puncta were labeled for STX13 as in WT melanocytes (Setty et al., 2007), a substantial fraction of TYRP1 was mislocalized to STX13-containing early endosomes in BLOC-2$^-$ (28 ± 7% overlap; Fig. 2, *a–f*, arrows) and melan-ru cells (22 ± 3%; Fig. S1, *a–d*). This degree of overlap was not as high as that observed in BLOC-1$^-$ cells (Setty et al., 2007). Moreover, a small but substantial fraction of TYRP1 overlapped with or surrounded the faint pigment granules in BLOC-2$^-$ cells observed by bright-field microscopy (Fig. 2 *c*, arrowheads; see Table 1 for quantification by electron microscopy). Consistently, melanosome localization of the peripheral cohort of ATP7A—a copper transporter that also requires BLOC-1 for melanosomal transport (Setty et al., 2008)—was reduced in BLOC-2$^-$ relative to BLOC-2^R cells (Fig. S1, *k–p*; and Fig. 3). As in WT melanocytes (Raposo et al., 2001; Setty et al., 2007), TYRP1 in BLOC-2$^-$ cells did not overlap appreciably in the periphery with either the lysosome marker LAMP2 (Fig. 2, *g–i*) or the early stage melanosome marker PMEL (Fig. S1, *e–g*), but overlapped extensively with the transiently expressed BLOC-1–dependent melanosome cargo, OCA2 (Fig. S1, *h–j*, arrowheads; Sitaram et al., 2012). These data indicate that in BLOC-2–deficient cells, BLOC-1–dependent cargoes are inefficiently delivered to melanosomes and are partially mislocalized to early endosomes.

In contrast to the obligate BLOC-1–dependent cargoes TYRP1, ATP7A, and OCA2, localization of the largely BLOC-1–independent TYR (Setty et al., 2007, 2008) was less severely altered in BLOC-2$^-$ cells. TYR accumulated abnormally in the perinuclear region (see next paragraph), but TYR distribution in the periphery to melanosomes was not substantially reduced in BLOC-2$^-$ cells relative to WT or BLOC-2^R cells, as best appreciated in the more highly pigmented cohort of BLOC-2$^-$ cells (Fig. 2, *j–o*; 37 ± 9% of TYR overlapped with pigment granules in WT, 32 ± 8% in BLOC-2$^-$, and 36 ± 8% in BLOC-2^R; differences were not statistically significant). Consistently, TYR activity in BLOC-2$^-$ cells, as determined by L-3,4-dihydroxyphenylalanine (DOPA; L-DOPA) histochemistry, was comparable to that of WT melanocytes and much higher than in control TYR-deficient cells. Post-fixation L-DOPA addition induced melanin accumulation primarily in melanosomes by electron microscopy (Fig. S2; D-DOPA control shows preexisting melanin), indicating that TYR was properly localized and active in vitro but less active in vivo. Thus, BLOC-2 function is limited to the BLOC-1–dependent pathway.

The IFM analyses also revealed a substantial accumulation of TYRP1, OCA2, ATP7A, and TYR near the microtubule-organizing center of BLOC-2–deficient melan-coa and melan-ru cells but not in BLOC-2^R cells (Fig. 2 and Fig. S1, large arrows); similar accumulation of LAMP2 was sometimes but not consistently observed. Because many compartments overlap in this region, we exploited quantitative immuno–electron

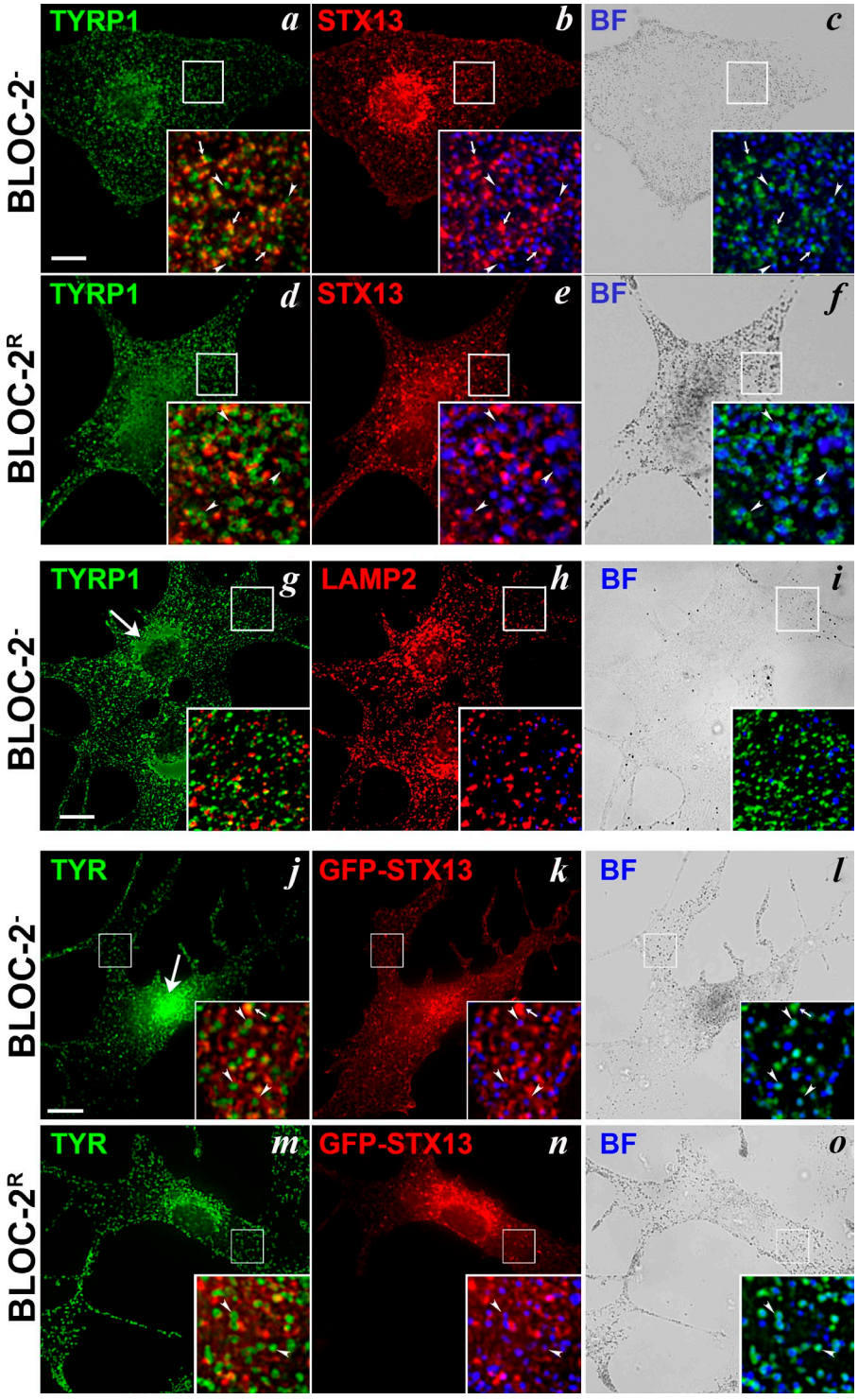

Figure 2. **TYRP1 but not TYR is partially mislocalized to early endosomes in the periphery of BLOC-2$^-$ cells.** (*a–o*) BLOC-2$^-$ (*a–c* and *g–l*) and BLOC-2^R (*d–f* and *m–o*) melanocytes were analyzed by deconvolution IFM after double labeling for TYRP1 (*a–i*) and STX13 (*a–f*) or LAMP2 (*g–i*), or transfection with EGFP-STX13 and labeling for TYR (*j–o*). Bright-field (BF) images are shown in *c*, *f*, *i*, *l*, and *o*. Insets, 3× (*j–o*) or 3.5× (all others) magnifications of the boxed regions as merged images with bright-field images pseudocolored blue. Arrows in insets, examples of overlap between TYRP1 or TYR and STX13 in BLOC-2$^-$ cells; arrowheads, examples of overlap between TYRP1 or TYR and pigment granules; large arrows, perinuclear accumulation of TYRP1 or TYR in BLOC-2$^-$ cells. Bars, 10 µm.

microscopy on ultrathin cryosections to better define the sites of TYRP1 accumulation. In BLOC-2^R melanocytes, as has been observed previously in WT melanocytes or MNT-1 melanoma cells (Raposo et al., 2001; Setty et al., 2007, 2008; Delevoye et al., 2009), immunogold labeling for TYRP1 was detected primarily on the limiting membrane of melanosomes with a smaller cohort on endosomal tubules and the Golgi (Fig. 3 *b* and Table 1). By comparison, TYRP1 labeling was reduced 2.4× on pigment granules (to 31.1%) and increased 1.6× on tubulovesicular and vacuolar endosomes in BLOC-2$^-$ cells (Fig. 3 *a* and Table 1), consistent with IFM results. Minor increases in TYRP1 labeling were also observed on multivesicular late endosomes and lysosomes (Table 1). Strikingly, TYRP1 labeling on the Golgi stacks was 6.5× higher in BLOC-2$^-$ relative to BLOC-2^R cells, representing nearly 20% of all TYRP1 (Fig. 3 and Table 1). Labeling for ATP7A was also substantially increased in the Golgi stacks and on tubulovesicular endosomes in BLOC-2$^-$ relative to BLOC-2^R cells, although sparse labeling on pigment granules

was detected in both cell types (Fig. 3). Thus, melanosomal cargoes of the BLOC-1 pathway are largely mislocalized to the Golgi and endosomes in the absence of BLOC-2.

EM analysis of BLOC-2$^-$ cells (Fig. 1, Fig. 3, and Fig. S2) failed to identify enlarged early endosomal vacuoles like those that accumulate in melanocytic cells that lack BLOC-1 (Setty et al., 2007, 2008) or are depleted of KIF13A or AP-1 (Delevoye et al., 2009). Moreover, TYRP1 and ATP7A accumulated less dramatically within vacuolar sorting endosomes than in BLOC-1–deficient cells (Setty et al., 2007, 2008). Thus, BLOC-2 does not likely function in cargo exit from endosomes but rather in a discrete step of cargo transport.

BLOC-2 antagonizes endocytic recycling of melanosomal cargoes

Besides the aberrant localization to early endosomes and the Golgi, TYRP1 levels at the plasma membrane—as assessed by flow cytometry—were increased (by 3.5–5-fold) in BLOC-2$^-$ and BLOC-2^{-C} relative to BLOC-2^R cells (Fig. 4 *a*), despite no significant change in total cellular TYRP1 expression (Fig. S3 *a*). Increased surface expression was specific for mature melanosome components because plasma membrane levels of the immature melanosome protein PMEL were only modestly increased (Fig. 4 *a*). Increased TYRP1 surface expression did not reflect reduced endocytosis, as TYRP1 endocytic rates (Setty et al., 2007; Truschel et al., 2009) were increased—not decreased—in BLOC-2$^-$, BLOC-2^{-C}, and melan-ru cells relative to rescued BLOC-2^R and melan-ru:HPS6 cells (Fig. 4 *b* and Fig. S3 *b*). Thus, another mechanism must account for high TYRP1 surface expression. Why TYRP1 endocytosis is accelerated in BLOC-2–deficient cells is unclear, but likely reflects alterations in membrane dynamics specifically during mature melanosomal cargo transport because endocytic rates for the premelanosomal protein PMEL (Fig. 4 *c*) and the nonmelanosomal transferrin receptor (TfR; Fig. 4 *d*) were either unaffected or decreased in BLOC-2$^-$ cells, respectively. Decreased TfR endocytic rates likely reflected increased TfR expression levels (Fig. 4 *a* and Fig. S3 *a*) and consequent competition for AP-2 binding by its tyrosine-based internalization signal (Marks et al., 1996; Warren et al., 1997) as also observed in BLOC-1$^-$ cells (Setty et al., 2007; Cullinane et al., 2011); in contrast, TYRP1 bears a dileucine-based internalization signal and likely engages a distinct saturable binding site on AP-2 (Marks et al., 1996; Kelly et al., 2008).

If TYRP1 endocytosis is not impaired in BLOC-2$^-$ cells, the high surface TYRP1 levels must reflect increased delivery to the plasma membrane. To probe TYRP1 flux through the plasma membrane, we monitored the rate at which fluorophore-conjugated anti-TYRP1 antibody in the culture medium was internalized and accumulated within cells (Setty et al., 2007). By this assay, TYRP1 traversed the plasma membrane at a substantially higher rate in BLOC-2$^-$ than BLOC-2^R cells, particularly

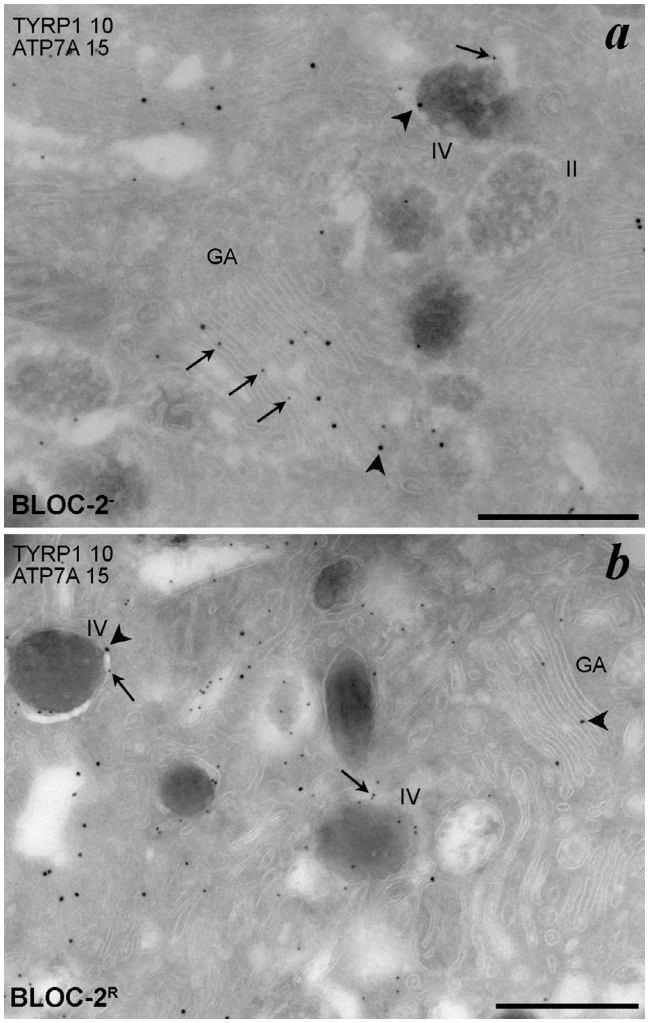

Figure 3. **TYRP1 accumulates in the Golgi of BLOC-2$^-$ melanocytes.** (*a* and *b*) Immunoelectron microscopy of ultrathin cryosections from BLOC-2$^-$ (*a*) and BLOC-2^R (*b*) melanocytes that were immunogold labeled for TYRP1 using10-nm protein A gold (TYRP1 10) and for ATP7A using 15-nm protein A gold (ATP7A 15). GA, Golgi apparatus; II and IV, stage II and IV melanosomes. Arrows show examples of TYRP1 labeling in the Golgi and stage IV melanosomes in BLOC-2$^-$ melanocytes (*a*) and on stage IV melanosomes in BLOC-2^R cells (*b*); note labeling on tubular and vacuolar endosomes in both cell types. Arrowheads show examples of ATP7A labeling on the Golgi and melanosomes in both cell types. Bars, 500 nm.

Table 1. **Quantification of TYRP1 immunogold labeling in BLOC-2$^-$ and BLOC-2^R melanocytes**

Cell	Golgi	TGN	Vac. End.	TVEs/End.	MVBs	Mels.	TVEs/Mel.	Lys.	Ves.
BLOC-2$^-$	**19.6**	7.7	7.0	10.8	6.7	**31.1**	9.1	4.0	4.0
BLOC-2^R	**3.0**	1.3	4.8	5.0	3.0	**74.2**	7.0	1.5	0.2

Ultrathin cryosections of BLOC-2$^-$ or BLOC-2^R cells were labeled with antibodies to TYRP1 and ATP7A and protein A conjugated to 10- and 15-nm gold particles, respectively. Gold particles decorating each indicated compartment were counted in ≥30 cell profiles each. Values are based on 1,278 gold particles counted in BLOC-2$^-$ cells and 1,430 in BLOC-2^R cells. Vac. End., vacuolar endosomes; TVEs, tubulovesicular endosomes near vacuolar endosomes or the Golgi (TVEs/End.) or near melanosomes (TVEs/Mel.); MVBs, multivesicular bodies; Mels, melanosome stages II, III, or IV; Lys., lysosomes; Ves., vesicles of undefined origin. Compartments with the most dramatic differences between cell lines are indicated in bold.

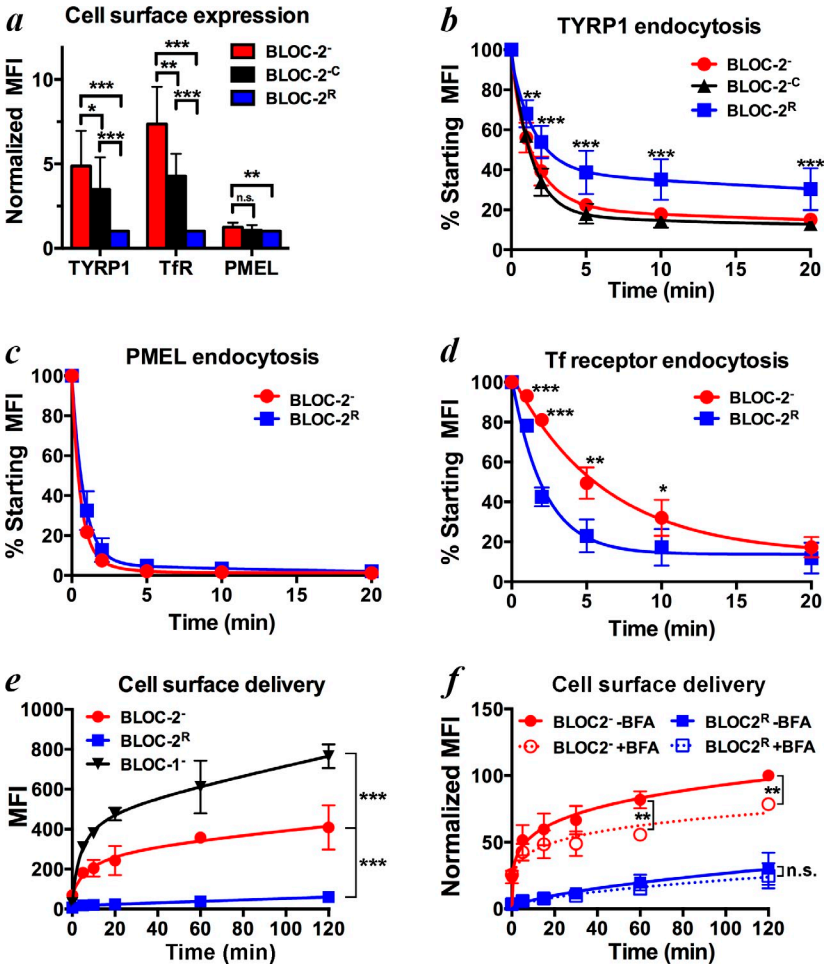

Figure 4. **Increased TYRP1 cycling through the plasma membrane in BLOC-2$^-$ melanocytes.** (*a*) Comparison of cell surface levels of TYRP1, TfR, or PMEL among BLOC-2$^-$, BLOC-2^{-C}, and BLOC-2^R melanocytes by flow cytometry after labeling of whole cells on ice with unlabeled primary and AF488-conjugated secondary antibody. The mean fluorescence intensity (MFI) ± SD over 4–15 experiments, each performed in duplicate or quadruplicate, was normalized to 1.0 for BLOC-2^R melanocytes within each experiment. (*b–d*) Quantification of TYRP1 (*b*), PMEL (*c*), and TfR (*d*) endocytosis rates. BLOC-2$^-$, BLOC-2^{-C}, or BLOC-2^R cells were incubated with unlabeled antibodies on ice and loss of surface antibody (detected with fluorescent secondary antibody) over time at 37°C was quantified by flow cytometry. MFI at each time point was calculated and plotted relative to MFI at time 0 (defined as 100%). Values (means ± SD) were from two to eight separate experiments performed in duplicate. (*b* and *d*) P-values are indicated for comparison of BLOC-2^R to BLOC-2$^-$ cells. Values in *c* were not significantly different. (*e* and *f*) Quantification of TYRP1 flux through the plasma membrane. Uptake of saturating levels of fluorescent anti-TYRP1 antibody by BLOC-2$^-$, BLOC-2^R, or BLOC-1–deficient melan-mu cells (BLOC-1$^-$) at 37°C was quantified over time by flow cytometry. In *f*, cells were left untreated or were treated with 10 µg/ml brefeldin A (BFA) for 1 h before and during the experiment as indicated. Values (means ± SD) were from at least three independent experiments performed either in duplicate or quadruplicate and represent raw MFI (*e*) or a normalized value (*f*) calculated as the percentage of the MFI value for untreated BLOC-2$^-$ cells at 2 h. P-values shown in *e* correspond to all points in the graph except the initial time point; p-values in *f* are shown only for differences deemed significant between −BFA and +BFA samples. *, P < 0.05; **, P < 0.01; ***, P < 0.001; n.s., not significant.

within the first 10 min (Fig. 4 *e*). The high plasma membrane sampling primarily reflected endocytic recycling rather than biosynthetic trafficking because the rate of accumulation was only modestly reduced by treatment with brefeldin A (BFA; Fig. 4 *f*), which does not affect TYRP1 recycling (Setty et al., 2007; Truschel et al., 2009). We thus conclude that TYRP1 undergoes excessive endocytic recycling in BLOC-2$^-$ cells. The misrouting through the cell surface in BLOC-2$^-$ cells was not as severe as in BLOC-1$^-$ melanocytes (Setty et al., 2007), affirming that BLOC-1 and BLOC-2 function at distinct steps in cargo transport.

BLOC-2 antagonizes retrograde trafficking of melanosomal cargoes to the Golgi

Because TYRP1 is delivered to melanosomes via recycling endosome carriers (Delevoye et al., 2009) to which BLOC-2 localizes (Di Pietro et al., 2006), increased TYRP1 endocytic recycling in BLOC-2$^-$ cells might reflect mistargeting of these carriers to the plasma membrane. Similar mistargeting to the Golgi might explain the increased Golgi accumulation of TYRP1 and other cargoes in BLOC-2$^-$ cells (Fig. 3). Consistently, the intensity of TYRP1 labeling within a "masked" Golgi region relative to the whole cell declined at a higher rate in WT (falling 26 ± 3% by 60 min and 31 ± 3% by 120 min) than in BLOC-2$^-$ cells (falling 18 ± 3% by 60 min and 20 ± 5% by 120 min) after inhibition of protein synthesis with cycloheximide (CHX; Fig. 5). Thus, either TYRP1 exits the Golgi more slowly in BLOC-2$^-$ cells or a smaller fraction of the Golgi cohort of TYRP1 in BLOC-2$^-$ cells is newly synthesized—consistent with an increase in recycling to the Golgi from endosomes.

To directly assess TYRP1 recycling to the Golgi, we used FRAP after expression of TYRP1-EGFP. TYRP1-EGFP faithfully reproduced TYRP1 localization, as it overlapped with pigment granules in WT melanocytes and with STX13-labeled early endosomes in BLOC-1$^-$ melanocytes to the same extent as endogenous TYRP1 (unpublished data). WT and BLOC-2$^-$ cells transiently expressing TYRP1-EGFP were treated for 60 min with CHX to clear newly synthesized TYRP1-EGFP from the Golgi. Using spinning-disk microscopy, the Golgi region (marked by coexpressed GM130-mCherry [mCh]) was bleached with a 488-nm laser and TYRP1-EGFP recovery in this region was monitored over time (Fig. 6, *a* and *b*; and Videos 1 and 2). Fluorescence recovery of TYRP1-EGFP in BLOC-2$^-$ cells was rapid and returned to ∼75% of the initial intensity over the course of 5 min; in contrast, recovery was negligible in WT cells (Fig. 6 *c*). Similar data were obtained by photobleaching only a small region of the Golgi (Fig. S3, *c* and *d*), suggesting that cargo diffusion within the stacks was minimal. Recovery in BLOC-2$^-$ cells was mediated by centripetal delivery of vesicles along tracks to the Golgi region (Video 2).

Thus, retrograde trafficking of TYRP1 to the Golgi is markedly enhanced in BLOC-2$^-$ cells.

To test whether increased retrograde trafficking in BLOC-2$^-$ cells was specific to melanosome cargoes, we used internalized Alexa Fluor 488 (AF488)–conjugated cholera toxin B subunit (CTxB; CTxB-AF488) as a probe (Sandvig et al., 2013). Cells were pulsed with CTxB-AF488, and accumulation within the Golgi region was monitored at different times by IFM. Unlike for TYRP1, the rate of CTxB-AF488 accumulation in the Golgi region over 4 h was significantly reduced in BLOC-2$^-$, BLOC-2^{-C}, and melan-ru cells compared with WT melan-Ink4a, BLOC-2^R, and rescued melan-ru:HPS6 melanocytes (Fig. 6, *d* and *e*). These data indicate that the increased retrograde trafficking in BLOC-2–deficient cells is specific to a melanosome cargo and not generalizable. The specific increases in TYRP1 trafficking to the plasma membrane and to the Golgi region are consistent with a model in which BLOC-2 diverts melanosome cargo from other destinations of recycling endosomes and toward melanosomes.

Stability and melanosome targeting of endosomal transport intermediates requires BLOC-2

We next considered whether BLOC-2 influences the dynamics of the recycling endosomal transport intermediates through which cargoes are delivered to maturing melanosomes (Delevoye et al., 2009). To visualize the intermediates, we exploited the pan-endosomal SNARE, STX13, tagged with EGFP or mCh. By immuno–electron microscopy, EGFP-STX13 expressed stably in human MNT-1 melanoma cells (in which the intermediates have been characterized; Delevoye et al., 2009) was detected on tubulovesicular structures and vacuolar endosomes with bilayered clathrin coats (Fig. 7, *a* and *b*), as observed for endogenous STX13 in other cell types (Prekeris et al., 1998; De Mazière et al., 2002). Labeling was particularly evident on tubules that emanated from vacuolar endosomes and that closely apposed and/or contacted melanosomes (Fig. 7, *c* and *d*), at least some of which were associated with AP-1 and/or contained TYRP1 (Fig. S4). Moreover, when expressed in WT mouse melanocytes and analyzed by live-cell spinning-disk microscopy, EGFP- or mCh-STX13 decorated vacuolar, punctate, and tubular structures with similar features as in MNT-1 cells (Fig. 7, *e–l*; and Fig. 8). Tubules labeled for both mCh-STX13 and GFP-RAB11A (enriched in recycling endosomes) emanated from puncta labeled by both mCh-STX13 and GFP-RAB5A (enriched on sorting endosomes; Fig. 7, *e–l*), as expected for the transport intermediates (Delevoye et al., 2009, 2014). Thus, EGFP- and mCh-STX13 label vacuolar endosomes and recycling endosomal tubular transport intermediates through which TYRP1 is transferred to melanosomes.

To visualize the transport intermediates relative to melanosomes, BLOC-2$^-$ or WT melanocytes that stably express EGFP-STX13 were transiently transfected with mRFP-tagged OCA2 to label melanosomes and analyzed by spinning-disk microscopy. In WT cells, the EGFP-STX13–labeled tubules were very dynamic (Fig. 8, *a* and *b*, arrowheads; and Video 3). Tubule length varied widely (Fig. 8 *c* and Video 4), but the majority of

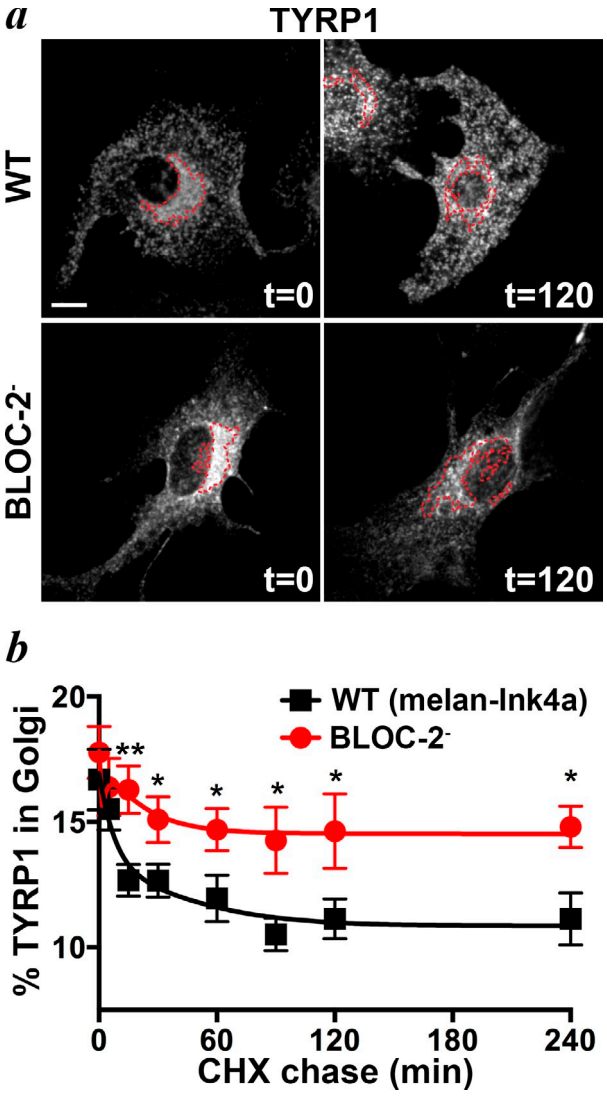

Figure 5. **TYRP1 that accumulates in the Golgi of BLOC-2$^-$ melanocytes is not newly synthesized.** WT melan-Ink4a or BLOC-2$^-$ cells on coverslips were treated with CHX at 37°C for the indicated times, and then fixed, labeled for TYRP1 and the Golgi marker giantin, and analyzed by IFM. (*a*) Representative deconvolved images of TYRP1 labeling at the 0 and 120 min time points. Red outline, Golgi region defined by giantin labeling. Bar, 10 µm. (*b*) The intensity of TYRP1 in the giantin-positive Golgi region was quantified relative to total TYRP1 fluorescence and plotted over time. Data represent means ± SD from ≥50 cells in three independent experiments. *, P < 0.05; **, P < 0.01.

tubules were longer than 1 µm (Fig. 8 *e*). Many tubules made transient contacts with melanosomes marked by mRFP-OCA2 (Fig. 8, *b* and *f*, arrow). These contacts lasted from a few seconds up to 60 s, with nearly half lasting longer than 20 s (Fig. 8, *b* and *g*). Qualitatively similar results were obtained using bright-field microscopy to visualize pigment granules relative to EGFP-STX13 (Fig. S5, *a* and *b*). These events reflect the previously described interactions between transport intermediates and melanosomes (Delevoye et al., 2009).

Relative to WT cells, similar numbers of EGFP-STX13–containing tubules were generated (Fig. 8, *a*, *b* [arrowheads], *c*, and *d*; and Videos 5 and 6) in BLOC-2$^-$ cells, but tubule length was significantly reduced such that the majority of tubules were

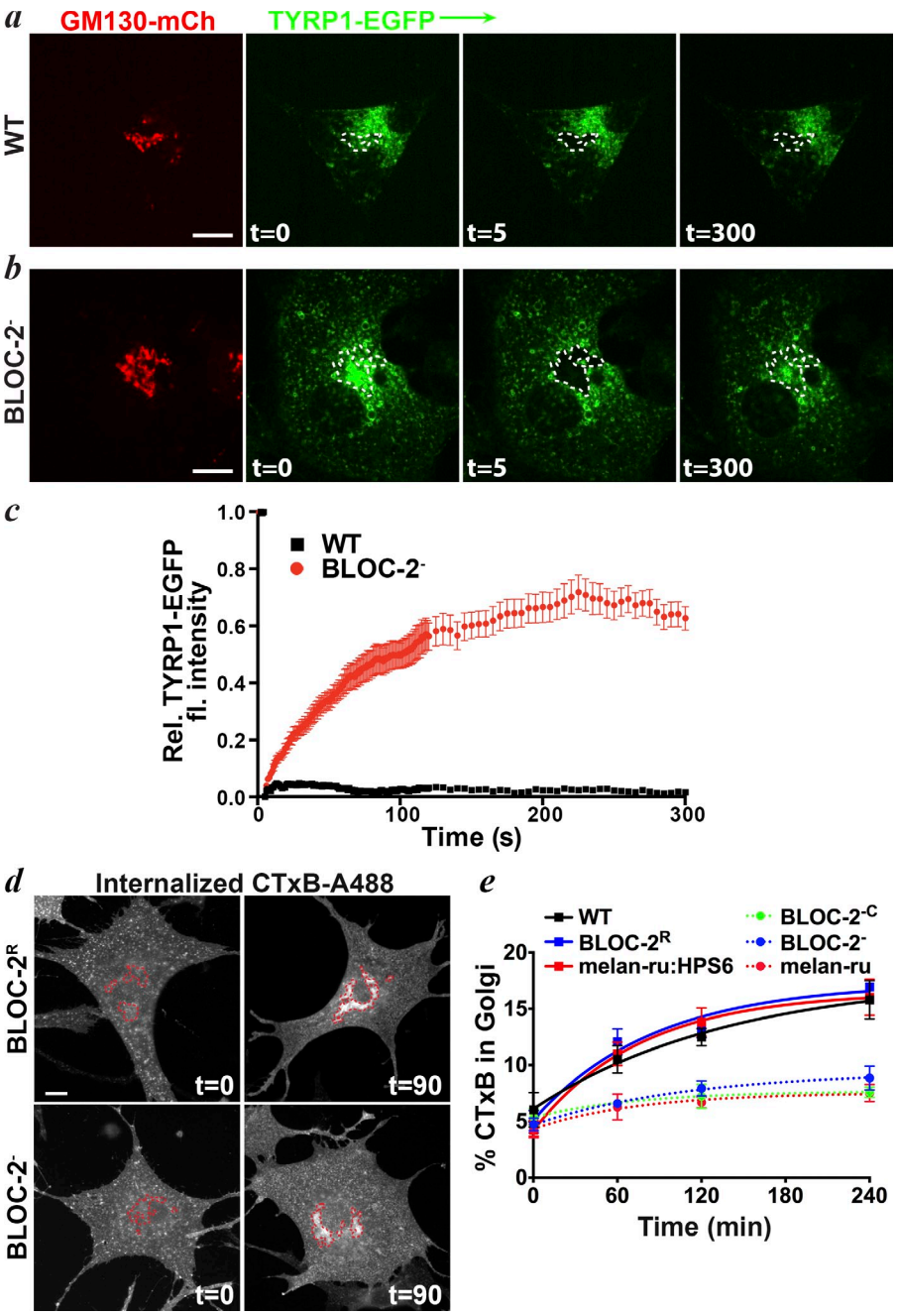

Figure 6. **Retrograde trafficking of TYRP1 to the Golgi is specifically increased in BLOC-2$^-$ melanocytes.** (*a–c*) WT melan-Ink4a or BLOC-2$^-$ cells transiently expressing TYRP1-EGFP and GM130-mCh to mark the Golgi, were pretreated with CHX for 60 min at 37°C and then imaged by spinning disk microscopy ($t = 0$). GFP fluorescence within the Golgi region labeled by GM130-mCh was bleached at frame 5 ($t = 5$), and recovery of TYRP1-EGFP fluorescence intensity was quantified over time by normalizing to prebleach GFP intensity of the same region. (*a* and *b*) Representative images for GM130-mCh and TYRP1-EGFP from $t = 0$, $t = 5$, and $t = 300$ (300 s) for WT (*a*) and BLOC-2$^-$ cells (*b*). Bleached region is indicated by the dotted white line in TYRP1-EGFP images. Bars, 10 µm. (*c*) Quantification of fluorescence recovery. Rel., relative; fl., fluorescence. Values represent the means ± SD of GFP intensity traces of 15 cells of each type. (*d* and *e*) WT (melan-Ink4a), "rescued" BLOC-2^R (melan-coa:hHPS3), or melan-ru:HPS6, or BLOC-2–deficient BLOC-2$^-$ (melan-coa), BLOC-2^{-C}, or melan-ru cells on coverslips were incubated with AF488-conjugated CTxB on ice for 1 h and then at 20°C for 15 min to allow for internalization. Cells were washed once and incubated at 37°C for the indicated times, fixed, labeled with the anti-giantin antibody and analyzed by IFM. (*d*) Representative CTxB fluorescence images of BLOC-2$^-$ and BLOC-2^R cells at the 0 and 90 min time points ($t = 0$, $t = 90$) showing appearance of CTxB in the Golgi (giantin staining; red outline) by 90 min. Bar, 10 µm. (*e*) Fluorescence intensity of AF488-CTxB in the giantin-positive region was quantified and plotted over time for all cell types. Values (means ± SD) for all BLOC-2–deficient lines are significantly different ($P < 0.01$ at 60 min and $P < 0.001$ at 120 and 240 min) from their paired BLOC-2–sufficient lines.

shorter than 1 µm (Fig. 8, *c* and *e*). Importantly, the frequency with which these tubules contacted mRFP-OCA2–labeled puncta was dramatically reduced in BLOC-2$^-$ cells (Fig. 8, *b* and *f*). For those tubules that did contact mRFP-OCA2–labeled puncta in BLOC-2$^-$ cells, the duration of contact was much shorter than in WT cells, such that >95% lasted fewer than 20 s (Fig. 8, *b* and *g*). Qualitatively similar results were obtained using bright-field microscopy to identify melanosomes (Fig. S5, *c* and *d*). The requirement for BLOC-2 in tubule dynamics was specific for the transport intermediates labeled by EGFP-STX13, as neither the number nor length of distinct tubules, labeled by GFP-VAMP8, was changed in BLOC-2–deficient melan-ru cells relative to rescued melan-ru:HPS6 cells (Fig. S5, *e–j*). Thus, endosome-derived tubules are less likely to establish and maintain contacts with melanosomes in the absence of BLOC-2. Together with the cargo localization and dynamics results, the data suggest that BLOC-2 favors melanosomal cargo delivery by specifying recycling endosomal transport intermediates to interact with maturing melanosomes.

Discussion

The protein complexes that are defective in most characterized HPS isoforms participate in cargo delivery to LROs such as melanosomes, but it was unknown how BLOC-2 functions. We show here that BLOC-2 facilitates the targeting of endosomal transport carriers specifically to melanosomes, averting "default" delivery to the plasma membrane and the Golgi—classical targets of recycling endosomes. These data are consistent with a role for BLOC-2 in mediating interactions between maturing

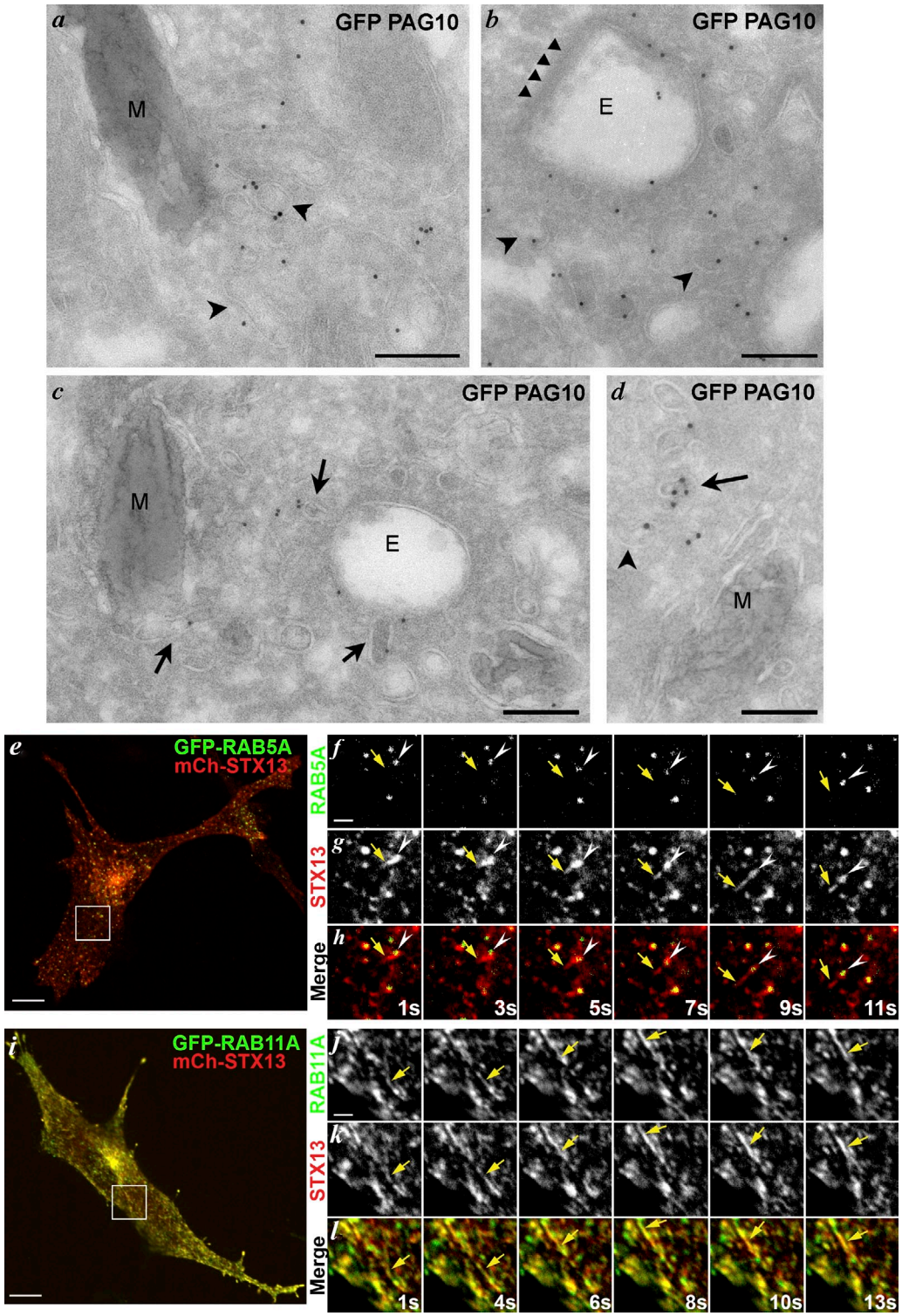

Figure 7. **EGFP-STX13 labels recycling endosomal-derived transport intermediates in melanocytic cells.** (*a–d*) Ultrathin cryosections of fixed human MNT-1 melanoma cells that stably express EGFP-STX13 were labeled with anti-GFP antibody and protein A conjugated to 10-nm gold particles (PAG10) and then analyzed by electron microscopy. Arrowheads point to vesicular structures associated with melanosomes (M; *a* and *d*) or endosomes (E; *b*); arrows (*c* and *d*) point to tubules that are continuous with endosomes or melanosomes; triangles (*b*) point to a bilayered clathrin coat on a vacuolar endosome. Bars, 200 nm. (*e–l*). WT melan-Ink4a mouse melanocytes were transiently transfected with mCh-STX13 and either GFP-RAB5A (*e–h*) or GFP-RAB11A (*i–l*) and analyzed 24 h later by spinning-disk confocal microscopy. (*e* and *i*) Single frames of representative cells showing overlap of mCh-STX13 with RAB5A-labeled vesicles (*e*) or RAB11A-labeled tubules (*i*). Bars, 10 µm. Image sequences from the boxed region in *e* and *i* are shown magnified 3× in *f–h* and *j–l*, respectively, with each label shown individually in black and white (*f*, *g*, *j*, and *k*) and merged images shown in color (*h* and *l*); elapsed time in seconds is indicated at bottom right. In *f–h*, an mCh-STX13–labeled tubule (yellow arrows) emerges from a GFP-RAB5–labeled punctate structure (white arrowheads). In *j–l*, a tubule (yellow arrows) is labeled for both mCh-STX13 and GFP-RAB11A. Bars, 2 µm.

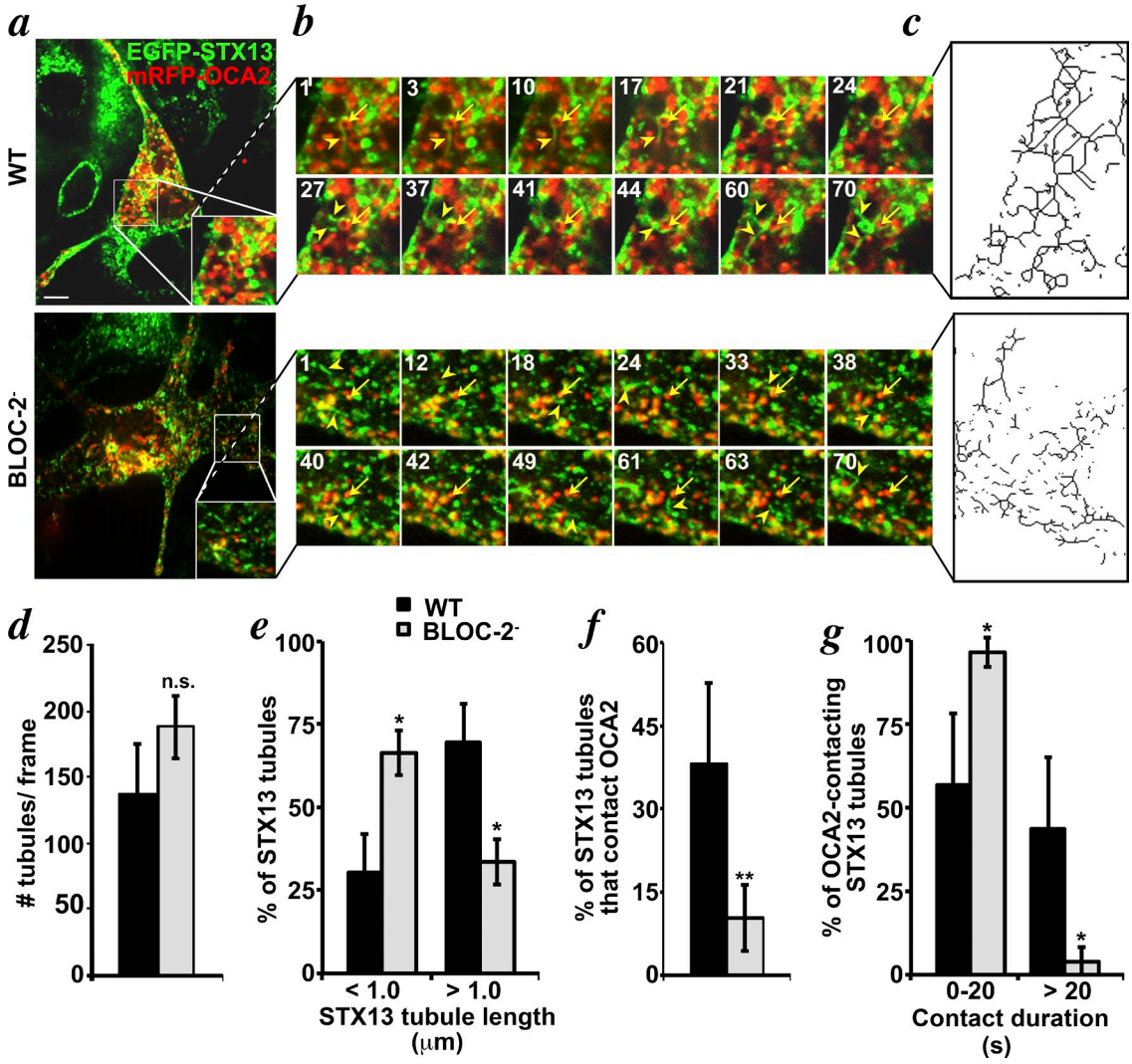

Figure 8. **BLOC-2 facilitates contacts of recycling endosomal tubules with maturing melanosomes.** WT melan-Ink4a and BLOC-2$^-$ cells stably expressing EGFP-STX13 were transfected with mRFP-OCA2 and imaged in a single plane at 1 fps for 5 min by spinning disk microscopy. (*a*) Starting frame from representative image series (Videos 3 and 5). Boxed region is magnified 2× in inset. Bar, 10 µm. (*b*) Frames from the image series of the magnified boxed region in *a* at the times (seconds) indicated in top left. Arrows, melanosomes that interact with tubules; arrowheads, examples of tubules. (*c*) EGFP-STX13 labeling in a single panel highlighted in *b* was analyzed using the ImageJ "skeletonize" function to emphasize tubule length (Videos 4 and 6 for image series). (*d*) The number of EGFP-STX13 tubules (branched structures in skeletonized images) per video frame using a constant frame size (12 × 12 µm) was quantified within at least five WT and BLOC-2$^-$ cells in each of three independent experiments. Shown is the mean number of tubules (±SD) identified in each frame. (*e*) The length of EGFP-STX13 tubules between vertices in skeletonized images was quantified within 10 WT and BLOC-2$^-$ cells each in three independent experiments. Shown are the percentages (means ± SD) of tubules with lengths shorter or longer than 1 µm. (*f*) The percentage of EGFP-STX13 tubules that contact mRFP-OCA2–positive compartments was quantified using a MATLAB program and averaged from five WT and BLOC-2$^-$ cells each in six independent experiments. Shown are the mean values ± SD. (*g*) For those EGFP-STX13 tubules that contact mRFP-OCA2 compartments, the duration of contact was quantified. Shown are the percentages of contacts (means ± SD) that lasted for greater or less than 20 s. *, P < 0.05; **, P < 0.01.

LROs and tubular recycling endosome-derived transport carriers ferrying LRO cargoes.

Our analyses of melanosome cargo distribution in BLOC-2–deficient melanocytes show a unique pattern of cargo mislocalization among HPS models. HPS 2, 8, and 9 models that lack AP-3 or BLOC-1 display defects in cargo exit from early endosomes into melanosome-bound transport carriers, resulting in altered early endosome morphology and cargo entrapment in early endosomes (Huizing et al., 2001; Theos et al., 2005; Setty et al., 2007, 2008; Delevoye et al., 2009). As in BLOC-1$^-$ cells (Setty et al., 2007; Cullinane et al., 2011), TYRP1 in BLOC-2$^-$ cells undergoes increased cycling to the plasma membrane and is modestly enriched in early endosomal compartments, likely as a result of repeated cycles of recycling and endocytosis. However, unlike in BLOC-1$^-$ cells, TYRP1 in BLOC-2$^-$ cells also accumulates in the Golgi; our FRAP and CHX chase analyses suggest that this cohort reflects increased retrograde trafficking. The primary sites of TYRP1 misaccumulation—the plasma membrane and the Golgi—are both targets of recycling endosomes in other cell types (Maxfield and McGraw, 2004; Bonifacino and Rojas, 2006). Because recycling endosomes serve as carriers through which TYRP1 is delivered to melanosomes (Delevoye et al., 2009), our data indicate that cargoes appropriately enter these transport carriers in BLOC-2$^-$ cells.

However, the carriers are largely diverted to other destinations, effectively reducing cargo delivery to melanosomes. This is distinct from the cargo transport defects in BLOC-1–deficient cells, in which TYRP1 fails to exit sorting endosomes (Setty et al., 2007, 2008; Cullinane et al., 2011) or in AP-1– or KIF13A-depleted cells in which the transport intermediates fail to form at all (Delevoye et al., 2009, 2014). The rapid movement of the carriers and lack of cargo accumulation in the vacuolar endosomes from which they originate likely explain why cargoes do not accumulate within the carriers themselves. Thus, our data support a model in which BLOC-1, AP-1, and KIF13A function during cargo exit from endosomes into transport carriers, and BLOC-2 facilitates the subsequent delivery of these carriers to melanosomes.

The results of our live-cell imaging analyses suggest that redirection of melanosome-bound cargo in BLOC-2$^-$ cells is caused by the loss of a specific interaction between endosomal cargo transport intermediates and maturing melanosomes. Whereas numerous recycling endosomal tubules in WT melanocytes underwent prolonged interactions with melanosomes marked by mRFP-OCA2 or pigmentation, such interactions were fewer and shorter in duration in BLOC-2$^-$ melanocytes. Although OCA2 is partially mislocalized in BLOC-2$^-$ melanocytes, tubule contacts with OCA2-labeled structures were more dramatically reduced than melanosome localization. The simplest explanation for these data is that BLOC-2 functions as a melanosome (or LRO)-specific tether for the tubular transport intermediates. This hypothesis is consistent with the immunolocalization of BLOC-2 to transferrin-containing recycling endosomal tubules (Di Pietro et al., 2006) and is supported by several observations. First, cargo delivery to melanosomes is impaired but not completely ablated in BLOC-2$^-$ cells, consistent with tethering defects in other systems and with the ability of SNAREs to function, albeit inefficiently, in the absence of tethering (Bröcker et al., 2010). Second, BLOC-2 is an effector of RAB32 and RAB38 and is recruited to membranes in part by RAB38 (Bultema et al., 2012); RAB32 and RAB38 function in membrane trafficking to melanosomes (Wasmeier et al., 2006; Bultema et al., 2012), and Rab interactions are a common feature of tethers (Bröcker et al., 2010). Third, TYR activity accumulates abnormally in vesicles in addition to melanosomes by electron microscopy of melanocytes from human HPS3 patients (Boissy et al., 2005), supporting a nonessential but important role in fusion of transport intermediates with target melanosomes. Finally, although BLOC-2 subunits lack sequence homology with known trafficking elements, tethering protein complexes often have poor sequence homology despite extensive structural similarity (Jackson et al., 2012). Other potential functions for BLOC-2 are possible but less consistent with our data. For example, BLOC-2 might function to stabilize the endosomal tubules rather than tether them; however, this would be less consistent with the more dramatic effects of BLOC-2 deficiency on the number and duration of contacts with melanosomes than on tubule length. Because the tubules that we observe likely require the plus end–directed kinesin-3 motor KIF13A for their formation (Delevoye et al., 2009, 2014), our data are not consistent with a proposed functional interaction between BLOC-2 and the dynein–dynactin complex (Li et al., 2014).

Our data suggest that BLOC-2 functions specifically on the tubular transport carriers observed here, which correspond to the TfR- and RAB11-enriched tubules described in human MNT-1 melanocytic cells (Delevoye et al., 2009) to which BLOC-2 has been localized (Di Pietro et al., 2006). As with those tubules (Delevoye et al., 2014), the tubules observed here emanate from vacuolar sorting endosomes and are enriched in recycling endosome markers such as STX13 and RAB11 but not in VAMP8, which marks a distinct class of dynamic membrane tubule that is not influenced by BLOC-2. They likely correspond to transport carriers specific to the BLOC-1–dependent pathway because the cargoes that are most depleted from melanosomes in BLOC-2$^-$ melanocytes—TYRP1, ATP7A, and OCA2—are obligate BLOC-1 cargoes (Setty et al., 2007, 2008; Sitaram et al., 2012). In contrast, TYR was only partially affected, as also observed in BLOC-1$^-$ cells (Setty et al., 2007, 2008) and indicated by its aberrant accumulation in the Golgi but near normal accumulation in melanosomes. This is also consistent with observations in melanocytes from HPS3 patients (Boissy et al., 2005). If BLOC-2 indeed functions as a tether as we hypothesize, we predict that a distinct tether functions for the BLOC-1–independent/AP-3–dependent delivery of TYR; because normal TYR localization and expression levels require RAB32 and RAB38 (Wasmeier et al., 2006; Bultema et al., 2012), such a tether would likely be another RAB32/38 effector.

Despite a substantial cohort of TYR within melanosomes in BLOC-2$^-$ cells and near normal levels of post-fixation TYR activity, BLOC-2$^-$ cells are nevertheless hypopigmented. Our observations that melanosomal transmembrane transporters such as OCA2 are mislocalized in BLOC-2$^-$ cells provide a potential explanation. OCA2 facilitates a chloride conductance that neutralizes intralumenal pH in maturing melanosomes, a requirement for TYR activity (Bellono et al., 2014). Reduced intralumenal pH, resulting from a reduced content of OCA2 and/or other transporters in melanosomes, would reduce TYR activity in vivo but not upon organelle permeabilization in vitro. Loss of transporter activity for an osmolyte, as predicted for the pigment cell-specific SLC45A2 proton-dependent sucrose transporter (Newton et al., 2001; Bartölke et al., 2014), might also explain why melanosomes in BLOC-2$^-$ melanocytes are unusually small (Suzuki et al., 2001; Zhang et al., 2003; Boissy et al., 2005; Helip-Wooley et al., 2007). Interestingly, unlike in BLOC-1$^-$ cells, sufficient levels of ATP7A are present in melanosomes in BLOC-2$^-$ melanocytes such that excess copper is not needed to observe copper-dependent TYR activity upon fixation. This is consistent with an ancillary role of BLOC-2 in cargo delivery as expected for a tether.

Materials and methods

Reagents

Chemicals were obtained from Sigma-Aldrich, except where noted. FuGENE 6, hygromycin B, and protease inhibitors were obtained from Roche. Tissue culture reagents, Matrigel, and Lipofectamine 2000 were obtained from Invitrogen. Protein A conjugated to 10- or 15-nm gold particles was from Cell Microscopy Center (Academisch Ziekenhuis Utrecht, Utrecht, Netherlands).

Cell culture and generation of stable cells

Immortal melanocyte cell lines melan-coa2 (HPS3 deficient; BLOC-2^{-}) derived from C57BL/10J *Hps3*$^{coa/coa}$ (*cocoa*) mice (Suzuki et al., 2001), melan-mu (BLOC-1 deficient) from B6.CHMU/Le *Muted*$^{mu/mu}$ (*muted*) mice (Setty et al., 2007), and WT melan-Ink4a-Arf-1 (formerly called melan-Ink4a-1; referred to here as melan-Ink4a or WT) from C57BL/6 *Ink4a-Arf*$^{-/-}$ mice (Sviderskaya et al., 2002) have been described and were derived from the skins of neonatal mice. The immortal melanocyte cell line melan-ru-1 (HPS6 deficient) was grown from skins of neonatal C57BL/6J *Hps6*$^{ru/ru}$ (*ruby eye*) mice after crossing to *Ink4a-Arf*$^{-/-}$ mice and selecting double homozygotes as previously described (Setty et al., 2007). All cells were cultured in RPMI 1640 medium supplemented with 10% FBS (Atlanta Biologicals) and 200 nM 12-*O*-tetradecanoylphorbol-13-acetate (Sigma-Aldrich). Retrovirus production from transiently transfected 293T cells or Plat-E cells (Morita et al., 2000), transduction, and selection of stable immortalized melanocyte cell lines with 200 µg/ml hygromycin were as previously described (Setty et al., 2007). Stable transfectants were occasionally treated with 200 µg/ml hygromycin B for 2–3 d to maintain selective pressure for the transgene. For FRAP experiments, cells were transiently transfected with pEGFP-N1-TYRP1-EGFP and GM130-mCh using Lipofectamine 2000 and imaged 24 h later. For live-cell imaging of STX13 relative to Rab proteins, cells were transiently transfected with pBMN-mCh-STX13 and either GFP-RAB5A or GFP-RAB11A and imaged 24 h later. For live cell imaging of STX13 tubules, stable cell lines expressing EGFP-STX13 from a pBMN retroviral vector were transiently transfected with pCR3-mRFP-OCA2-HA and visualized after 48 h. Stable transductants of human MNT-1 melanoma cells expressing EGFP-STX13, cultured as previously described (Raposo et al., 2001), were generated by recombinant retroviral transduction and selection with 200 µg/ml hygromycin.

Antibodies

The following monoclonal antibodies were used: mouse anti-TYRP1 (TA99) and anti-MYC epitope (9E10) were obtained from ATCC; rat anti–mouse LAMP1 (1D4B) and LAMP2 (GL2A7) were obtained from Developmental Studies Hybridoma Bank (University of Iowa, Iowa City, IA); mouse anti-PMEL (HMB-45, used for IFM) was purchased from Lab Vision; rat anti–mouse TfR (CD71, used for endocytosis and recycling assays) was obtained from BD; mouse anti–human TfR (H68.4, used for immunoblotting) was purchased from BioGenex; mouse anti-HA.11 was purchased from Covance; and mouse anti–γ-adaptin (100/3) and mouse anti–γ-tubulin (GTU88) were purchased from Sigma-Aldrich. Polyclonal rabbit antisera to HPS6 (a gift from V. Faundez, Emory University, Atlanta, GA; Gautam et al., 2004), STX13 (Prekeris et al., 1998), ATP7A (Setty et al., 2008), TYR (Calvo et al., 1999), and the N terminus of mouse PMEL (used for the endocytosis assay; Theos et al., 2006) have been described previously. Rabbit anti-giantin was obtained from Abcam (ab24586); rabbit anti-MYC (C-14) and anti-TYRP1 (H-90), used for immunoblotting, were obtained from Santa Cruz Biotechnology, Inc.; and rabbit anti-GFP was purchased from Invitrogen. Species- and/or mouse isotype–specific secondary antibodies from donkey or goat conjugated to AF488, Alexa Fluor 594, phycoerythrin, or DyLight 488 or 594 used in IFM and flow cytometry or conjugated to alkaline phosphatase for immunoblotting were either obtained from Invitrogen or Jackson ImmunoResearch Laboratories, Inc. Purified TA99 anti-TYRP1 antibody was conjugated to AF488 using a kit from Invitrogen.

DNA constructs

The retroviral construct pBMN-hHPS3-IRES-Hygro N/X encoding human HPS3 (hHPS3) under the control of the Maloney murine leukemia virus (MMLV) promoter was generated by subcloning the NotI–XbaI cDNA fragment from hHPS3/pCMV6-XL5 (obtained from OriGene; IMAGE [Integrated Molecular Analysis of Genomes and their Expression] ID TC127283; GenBank accession no. NM_032383) into the pCI vector (Promega), and then subcloning the resulting NotI–XhoI fragment into the MMLV-based retroviral vector pBMN-IRES-Hygro N/X (Setty et al., 2007). MMLV-based retroviral vectors encoding mouse HPS5 and HPS6 were generated by subcloning the SalI–NotI cDNA fragments (mHPS5-IMAGE ID 6405811 and mHPS6-IMAGE ID 3673655 obtained from ATCC) directly into the XhoI–NotI sites of pBMN-IRES-Hygro X/N. pBMN-MuHA encoding HA-tagged human Muted controlled by the MMLV promoter was previously described (Setty et al., 2007). EGFP-STX13 was generated by amplifying the coding region for human Syntaxin 12 (also known as STX13; obtained from ATCC: IMAGE ID 3851266), flanked by BamH1 and XhoI sites and subcloning into the BglII–SalI sites of pEGFP-C1 (Takara Bio Inc.), and is controlled by the human cytomegalovirus (CMV) immediate early promoter. The EGFP-STX13 fusion was then amplified flanked by BamH1 and XhoI sites and subcloned into the MMLV-based pBMN-IRES-Hygro X/N retroviral vector to generate pBMN-EGFP-STX13. mCH-STX13 controlled by the CMV promoter was generated by subcloning mCh into pEGFP-C1-STX13 using the AgeI–BsrGI region of mCh from pmCh-C1 (Takara Bio Inc.). TYRP1-EGFP controlled by the CMV promoter was generated by amplifying the human TYRP1 cDNA from pCDNA3-TRP1 (a gift from W. Storkus, University of Pittsburgh, Pittsburgh, PA) flanked with EcoRI and SalI sites and subcloning into pEGFP-N1 (Takara Bio Inc.). An XhoI–NotI fragment encompassing the TYRP1-EGFP fusion was then subcloned into pBMN-IRES-Hygro X/N to generate the retroviral pBMN-TYRP1-EGFP vector under the control of the MMLV promoter. To generate pCR3-mRFP-OCA2 in which mRFP-OCA2 is expressed from the CMV promoter, mRFP with flanking BamHI and Acc65I sites was subcloned from pCMV-mRFP (a gift from R. Tsien, University of California, San Diego, La Jolla, CA via G. Koretzky, Weill Cornell Medical College, New York, NY) into the coding region for the N terminus of OCA2 with a lumenal HA epitope in pCR3-OCA2-HA (Sitaram et al., 2009). GM130-mCh controlled by the CMV promoter was a gift from J. Lippincott-Schwartz (National Institutes of Health, Bethesda, MD). GFP-VAMP8 in pEGFP-C vector, controlled by the CMV promoter and generated from mouse cDNA, was a gift from P. Roche (National Institutes of Health, Bethesda, MD). GFP-RAB5A and -RAB11A encoding human RAB isoforms in pEGFP-C vectors and controlled by the CMV promoter were gifts from B. Goud (Institut Curie, Paris, France).

Electron microscopy

For conventional electron microscopy analyses, cells were fixed with 2% paraformaldehyde and 1% glutaraldehyde, post-fixed with osmium tetroxide and ferrocyanide and embedded in Epon, and ultrathin sections were prepared with an ultramicrotome (Reichert UltracutS; Leica) as previously described (Raposo et al., 2001). DOPA immunohistochemistry analysis was performed on cells fixed for 1–2 h in Karnovsky's fixative and 0.5% glutaraldehyde by incubation with 0.1% (wt/vol) L-DOPA (or D-DOPA as a negative control) in cacodylate buffer followed by fixation as previously described (Setty et al., 2008) and processing as outlined above. For immunoelectron microscopy, cells were fixed with 2% paraformaldehyde and 0.2% glutaraldehyde, embedded in 10% (wt/vol) gelatin, infused in 2.3 M sucrose, and frozen in liquid nitrogen as previously described (Raposo et al., 1997). Ultrathin cryosections were prepared with an ultracryomicrotome (Ultracut FCS; Leica) as previously described (Raposo et al., 1997) and single or double immunogold labeled with antibodies and protein A coupled to 10- or 15-nm gold particles. Sections were analyzed on an electron microscope (Philips CM120; FEI) using a digital numeric camera (Keen View; Soft Imaging System). Quantification of immunogold labeling on different organelles was performed as previously described (Theos et al., 2005). In brief, gold particles associated with the indicated compartments, defined morphologically, were counted in ≥30 different profiles of each cell type on at least two grids. Golgi, lysosomes, melanosomes (stages II–IV), multivesicular bodies (with more than three internal vesicles), and vacuolar endosomes (with three or less internal vesicles) were defined by classical morphological features; tubulovesicular elements were characterized as near vacuolar endosomes or melanosomes. The data in Table 1 represent the mean percentage of gold particles in each compartment over at least two separate experiments.

Flow cytometry

Cell surface expression, endocytosis, and cell surface delivery assays were performed as described previously (Setty et al., 2007) using flow cytometry on a FACScan or FACSCalibur instrument and CellQuest Pro software (BD). In brief, for cell surface labeling, cells in suspension were labeled on ice with primary and fluorophore-conjugated secondary antibodies and analyzed directly by flow cytometry. To quantify endocytosis, unlabeled antibody was bound to the surface of cells in suspension in ice, and cells were warmed to 37°C for various periods of time to allow endocytosis. Loss of surface-bound antibody was quantified using a fluorophore-conjugated secondary antibody and flow cytometry analysis. For cell surface delivery, cells were incubated with growth medium containing AF488-conjugated anti-TYRP1 antibody for 30 min on ice and then additionally at 37°C for various periods of time before washing and flow cytometry analysis. In some experiments, 10 µg/ml BFA was included during a 60-min preincubation and throughout the experiment to block biosynthetic cargo delivery.

Immunoblotting

Whole cell lysates were fractionated by SDS-PAGE and analyzed by immunoblotting with alkaline phosphatase–conjugated secondary antibodies

and enhanced chemiluminescence detection as previously described (Berson et al., 2000). In brief, whole cell lysates prepared by boiling in 1% SDS and sonication were fractionated by SDS-PAGE. After electrotransfer to polyvinylidene difluoride membranes and blocking in Blotto (PBS/5% milk/0.1% Tween 20), membranes were probed sequentially (with washing in between with PBS) with primary antibodies and alkaline phosphatase–conjugated goat anti–rabbit immunoglobulin antibody, each diluted in Blotto. Blots were developed using ECF enhanced chemifluorescence and detected using a phosphorimager (Storm 860; Molecular Dynamics) with ImageQuant software (GE Healthcare).

Fluorescence microscopy

Standard IFM and colocalization analyses. Cells were plated on Matrigel (BD)-coated coverslips, fixed with 2% formaldehyde, labeled with primary and secondary antibodies, mounted in Fluoromount-G (SouthernBiotech), and analyzed on a microscope (DM IRBE; Leica) equipped with a 63× or 100× Plan Apochromat objective lens (Leica; both 1.4 NA) and either an Orca 100 (Hamamatsu Photonics) or a Retiga EXi Fast 1394 (QImaging) digital camera as described previously (Setty et al., 2007). Images in sequential z planes were captured, deconvolved, analyzed, and manipulated using OpenLab (PerkinElmer) software and subtractive volume deconvolution. Quantification of the area of overlap in the cell periphery between markers in double labeling experiments was performed as described previously (Setty et al., 2007). In brief, deconvolved single-plane images of cells (captured at 63×) labeled for each marker in ≥10 cell profiles for each comparison were rendered binary by density slicing using OpenLab software; the intensely labeled perinuclear region was excluded; the total labeled area in each channel was calculated for objects larger than 5 pixels; an overlap image was calculated using the "AND" function, and the total area of overlap was calculated for objects larger than 5 pixels; and the percentage of overlap was defined as the total area of overlap divided by the total area labeled in the reference channel. Quantification of the area of overlap in the cell periphery between TYR and pigmented melanosomes was carried out using ImageJ (http://fiji.sc/Fiji; National Institutes of Health) on wide-field fluorescence images acquired at 63×. In brief, binary images of fluorescence (TYR labeling) were generated by subtracting the local background before thresholding using parameters of a rolling ball radius of 10 pixels with smoothing disabled, and binary images of pigment granules from bright-field imaging were generated by manual thresholding. The Image Calculator function was used to multiply the binary images for bright-field melanosomes and TYR staining; the resulting image represents the area of overlap between TYR staining and melanosomes. The areas of overlap and of total TYR labeling in structures larger than 5 pixels were quantified using the Analyze Particles function; the ratio of overlap pixels to total TYR pixels gives the percentage of overlap.

TYRP1 depletion from the Golgi. WT melan-Ink4a and BLOC-2$^-$ melanocytes plated on Matrigel-coated coverslips 24 h earlier were incubated with 300 µg/ml CHX at 37°C for the indicated times. Cells were then fixed by addition of an equal volume of 6% paraformaldehyde in HBSS and processed for IFM analysis as described under Standard IFM and colocalization analyses using a 40× Neofluor objective lens. TYRP1 fluorescence intensity within a masked region identified by giantin labeling was quantified using Volocity software (PerkinElmer). Images shown in Fig. 5 were captured as described for colocalization analyses.

FRAP. WT and BLOC-2$^-$ cells were plated on Matrigel-coated 35-mm glass-bottom dishes (MatTek Corporation) and transiently transfected to express TYRP1-EGFP and GM130-mCh. 24 h after transfection, cells were pretreated with 300 µg/ml CHX in culture medium at 37°C for 60 min and imaged using a spinning-disk confocal microscope (UltraVIEW; PerkinElmer) equipped with a 63× Plan Apochromat lens (Carl Zeiss), a camera (Orca-ER; Hamamatsu Photonics), an environmental chamber kept at 37°C, and Volocity software (PerkinElmer). Images were captured at 1 frame per second (fps) for 2 min and an additional 3 min at 1 frame per 5 s. At frame 5 (corresponding to 5 s of imaging), a region defined as GM130-mCh positive was bleached for GFP with a PhotoKinesis device (PerkinElmer). Fluorescence intensity of TYRP1-EGFP was quantified using ImageJ and normalized to mean prebleach GFP intensity within the bleached region and corrected for loss of fluorescence in an unbleached region.

CTxB retrograde trafficking. For CTxB uptake, WT, BLOC-2$^-$, BLOC-2^R, BLOC-2^C, melan-ru, or melan-ru:HPS6 cells plated on Matrigel-coated coverslips 24 h earlier were incubated on ice for 1 h with AF488-conjugated CTxB (2 mg/ml; Sigma Aldrich) in complete medium. Cells were then warmed to 20°C for 15 min to allow internalization, and then washed three times with ice cold medium and incubated for 15–240 min at 37°C. Cells were processed for IFM analysis as described for TYRP1 Golgi depletion.

Live-cell imaging of EGFP-STX13–, mCH-STX13–, EGFP-RAB5A–, EGFP-RAB11A–, and EGFP-VAMP8–expressing cells. WT or BLOC-2$^-$ cells were plated on Matrigel-coated 35-mm glass-bottom dishes and transiently transfected with EGFP-STX13, mCH-STX13, EGFP-RAB5A, EGFP-RAB11A, and/or EGFP-VAMP8 as indicated using Lipofectamine 2000. 24 h after transfection, cells in culture medium were imaged on a spinning-disk confocal microscope (UltraVIEW) equipped with an environmental chamber at 37°C, a camera (Orca ER), and Volocity for image acquisition. All images were captured at 1 fps.

Live-cell imaging of EGFP-STX13 stable cells. WT or BLOC-2$^-$ cells stably expressing EGFP-STX13 were plated on Matrigel-coated 35-mm glass-bottom dishes and transiently transfected to express mRFP-OCA2. Cells were visualized by spinning-disk confocal microscopy equipped with an environmental chamber at 37°C/5% CO_2. Time-lapse microscopy was performed by capturing images over 5 min at 1 fps using a spinning-disk microscope (IX71; Olympus) equipped with an electron multiplying charge-coupled device camera (ImagEM; Hamamatsu Photonics) and IPLab (BD) or MetaMorph (Molecular Devices) software. Image sequences were further analyzed either with ImageJ or MATLAB (MathWorks, Inc.) software. Images were processed into binary and skeletonized, and tubule length and number were quantified from each skeletonized video frame (equal frame area in each video) using the Analyze Particles plugin in ImageJ software. Values were averaged per video. Tracking of EGFP-STX13 and mRFP-OCA2 merging and splitting events was performed with MATLAB software applying a modified version of a previously described algorithm (supplemental material; Jaqaman et al., 2008).

Quantification of EGFP-VAMP8 tubules. To measure tubule number and length, images were cropped within ImageJ to remove adjacent cells and the nuclear region of each analyzed cell, and then converted to a binary image and skeletonized. The skeletonized image series was quantified using the Analyze Skeleton plugin. Features with a mean branch length of 5–50 pixels were included in the analysis. For analysis of tube number per area, the total cell area was measured in ImageJ and used for normalization.

Statistical analysis

Statistical significance was determined by the unpaired Student's *t* test and analysis of variance. *, $P < 0.05$; **, $P < 0.01$; and ***, $P < 0.001$.

Online supplemental material

Fig. S1 shows colocalization analyses of: TYRP1 with STX13 in a second BLOC-2–deficient line (melan-ru); TYRP1 with PMEL and with OCA2-HA in BLOC-2$^-$ cells; and ATP7A with pigment granules in BLOC-2$^-$ and BLOC-2^R cells. Fig. S2 shows tyrosinase activity and protein expression levels in BLOC-2$^-$ and BLOC-2^R cells. Fig. S3 shows expression levels of relevant proteins in BLOC-2$^-$, BLOC-2^{-C}, and BLOC-2^R cells, TYRP1 endocytic rates in melan-ru and melan-ru:HPS6 cells, and a FRAP analysis of a small region of the Golgi in WT and BLOC-2$^-$ cells. Fig. S4 shows immunoelectron microscopy analysis of EGFP-STX13 relative to TYRP1 or AP-1 in MNT-1 cells. Fig. S5 shows live-cell imaging of WT and BLOC-2$^-$ cells by alternating bright field and fluorescence microscopy to visualize GFP-STX13 relative to pigment granules, and of rescued melan-ru:HPS6 and BLOC-2–deficient melan-ru cells to visualize and quantify GFP-VAMP8–containing tubules. Videos 1 and 2 show recovery of TYRP1 fluorescence intensity in the Golgi after photobleaching in WT and BLOC-2$^-$ cells, respectively. Video 3 and 5 show live imaging of WT (Video 3) or BLOC-2$^-$ (Video 5) melanocytes expressing both EGFP-STX13 and mRFP-OCA2. Videos 4 and 6 show skeletonized trajectories of EGFP-STX13 in WT (Video 4) or BLOC-2$^-$ (Video 6) melanocytes. The source code for the MATLAB software used to quantify the interaction of EGFP-STX13 and mRFP-OCA2 in Fig. 8, modified from Jaqaman et al., 2008, is provided online as a ZIP file and contains the following files. Colorutrack notes.txt provides a brief description of how to use the script. colorutrack.m is the central script used to select the series of images to be analyzed, and calls the detection and tracking scripts. matchpoints.m processes the results of colorutrack.m (TrackingG.mat, TrackingR.mat, trackfinal_g.mat, and trackfinal_r.mat), extracts the x and y positions and amplitude of each tracked feature, and then searches for the feature within each frame of the image sequence. eventInfo.m uses data files produced by colorutrack and matchpoints to count discrete events (in this case, contacts between red and green features) and count the duration (number of frames) of each discrete event. /example_data_for_matchpoints.m/movieInfo_g.mat and /example_data_for_matchpoints.m/movieInfo_r.mat provide sample movieInfo data produced by colocation.m for a green channel and a red channel, respectively, to be used with the matchpoints script. /example_data_for_matchpoints.m/tracksfinal_g.mat

and /example_data_for_matchpoints.m/tracksfinal_r.mat provide sample tracking data produced by colocation.m for a green channel and a red channel, respectively, to be used with the matchpoints script. plotTracksGreen.m and plotTracksRed.m are utilities to extract and plot the x, y data for the green channel and for the red channel, respectively, from tracksCoordAmpCG. (tracksCoordAmpCG is output of scriptTrackGeneral as part of tracksFinal.) utrack.m combines Jaqaman's scriptDetectGeneral and scriptTrackGeneral and is called by colorutrack. colocation.m is a utility to find closely spaced locations of moving particles in red and green layers. Online supplemental material is available at http://www.jcb.org/cgi/content/full/jcb.201410026/DC1.

We thank V. Faundez, R. Tsien, G. Koretzky, W. Storkus, A. Linstedt, P. Roche, B. Goud and J. Lippincott-Schwartz for generous gifts of reagents; A. Stout and the University of Pennsylvania Cell and Developmental Biology Department core microscopy facility and J. Burkhardt and her laboratory for technical assistance with spinning-disk microscopy; the Penn Vision Research Center for live imaging analysis; and the Penn Flow Cytometry and Cell Sorting Resource Facility.

This work was supported by National Institutes of Health grants R01 EY015625 (to M.S. Marks and G. Raposo) and P30 EY001583 from the National Eye Institute and R01 GM108807 from the National Institute of General Medical Sciences (to M.S. Marks), the Institut Curie and Centre National de la Recherche Scientifique (to G. Raposo), Wellcome Trust grant 078327 (to E.V. Sviderskaya and D.C. Bennett), postdoctoral fellowship 0625437U from the American Heart Association and Wellcome Trust–Department of Biotechnology India Alliance Senior Fellowship 500122/Z/09/Z (to S.R.G. Setty), and Institutional Research and Academic Career Development Award postdoctoral fellowship K12 GM081259 and National Institutes of Health grant F32 AR062476 (to M.K. Dennis).

The authors declare no competing financial interests.

Submitted: 7 October 2014
Accepted: 20 April 2015

References

Bartölke, R., J.J. Heinisch, H. Wieczorek, and O. Vitavska. 2014. Proton-associated sucrose transport of mammalian solute carrier family 45: an analysis in *Saccharomyces cerevisiae*. *Biochem. J.* 464:193–201. http://dx.doi.org/10.1042/BJ20140572

Bellono, N.W., I.E. Escobar, A.J. Lefkovith, M.S. Marks, and E. Oancea. 2014. An intracellular anion channel critical for pigmentation. *eLife*. 3:e04543. http://dx.doi.org/10.7554/eLife.04543

Berson, J.F., D.W. Frank, P.A. Calvo, B.M. Bieler, and M.S. Marks. 2000. A common temperature-sensitive allelic form of human tyrosinase is retained in the endoplasmic reticulum at the nonpermissive temperature. *J. Biol. Chem.* 275:12281–12289. http://dx.doi.org/10.1074/jbc.275.16.12281

Boissy, R.E., B. Richmond, M. Huizing, A. Helip-Wooley, Y. Zhao, A. Koshoffer, and W.A. Gahl. 2005. Melanocyte-specific proteins are aberrantly trafficked in melanocytes of Hermansky-Pudlak syndrome-type 3. *Am. J. Pathol.* 166:231–240. http://dx.doi.org/10.1016/S0002-9440(10)62247-X

Bonifacino, J.S., and R. Rojas. 2006. Retrograde transport from endosomes to the trans-Golgi network. *Nat. Rev. Mol. Cell Biol.* 7:568–579. http://dx.doi.org/10.1038/nrm1985

Bröcker, C., S. Engelbrecht-Vandré, and C. Ungermann. 2010. Multisubunit tethering complexes and their role in membrane fusion. *Curr. Biol.* 20:R943–R952. http://dx.doi.org/10.1016/j.cub.2010.09.015

Bultema, J.J., A.L. Ambrosio, C.L. Burek, and S.M. Di Pietro. 2012. BLOC-2, AP-3, and AP-1 proteins function in concert with Rab38 and Rab32 proteins to mediate protein trafficking to lysosome-related organelles. *J. Biol. Chem.* 287:19550–19563. http://dx.doi.org/10.1074/jbc.M112.351908

Calvo, P.A., D.W. Frank, B.M. Bieler, J.F. Berson, and M.S. Marks. 1999. A cytoplasmic sequence in human tyrosinase defines a second class of dileucine-based sorting signals for late endosomal and lysosomal delivery. *J. Biol. Chem.* 274:12780–12789. http://dx.doi.org/10.1074/jbc.274.18.12780

Cheli, V.T., and E.C. Dell'Angelica. 2010. Early origin of genes encoding subunits of biogenesis of lysosome-related organelles complex-1, -2 and -3. *Traffic*. 11:579–586. http://dx.doi.org/10.1111/j.1600-0854.2010.01044.x

Cullinane, A.R., J.A. Curry, C. Carmona-Rivera, C.G. Summers, C. Ciccone, N.D. Cardillo, H. Dorward, R.A. Hess, J.G. White, D. Adams, et al. 2011. A BLOC-1 mutation screen reveals that PLDN is mutated in Hermansky-Pudlak Syndrome type 9. *Am. J. Hum. Genet.* 88:778–787. http://dx.doi.org/10.1016/j.ajhg.2011.05.009

Daly, C.M., J. Willer, R. Gregg, and J.M. Gross. 2013. snow white, a zebrafish model of Hermansky-Pudlak Syndrome type 5. *Genetics*. 195:481–494. http://dx.doi.org/10.1534/genetics.113.154898

Delevoye, C., I. Hurbain, D. Tenza, J.-B. Sibarita, S. Uzan-Gafsou, H. Ohno, W.J.C. Geerts, A.J. Verkleij, J. Salamero, M.S. Marks, and G. Raposo. 2009. AP-1 and KIF13A coordinate endosomal sorting and positioning during melanosome biogenesis. *J. Cell Biol.* 187:247–264. http://dx.doi.org/10.1083/jcb.200907122

Delevoye, C., S. Miserey-Lenkei, G. Montagnac, F. Gilles-Marsens, P. Paul-Gilloteaux, F. Giordano, F. Waharte, M.S. Marks, B. Goud, and G. Raposo. 2014. Recycling endosome tubule morphogenesis from sorting endosomes requires the kinesin motor KIF13A. *Cell Reports*. 6:445–454. http://dx.doi.org/10.1016/j.celrep.2014.01.002

Dell'Angelica, E.C. 2004. The building BLOC(k)s of lysosomes and related organelles. *Curr. Opin. Cell Biol.* 16:458–464. http://dx.doi.org/10.1016/j.ceb.2004.05.001

Dell'Angelica, E.C., C. Mullins, S. Caplan, and J.S. Bonifacino. 2000. Lysosome-related organelles. *FASEB J.* 14:1265–1278. http://dx.doi.org/10.1096/fj.14.10.1265

De Mazière, A.M., K. Muehlethaler, E. van Donselaar, S. Salvi, J. Davoust, J.-C. Cerottini, F. Lévy, J.W. Slot, and D. Rimoldi. 2002. The melanocytic protein Melan-A/MART-1 has a subcellular localization distinct from typical melanosomal proteins. *Traffic*. 3:678–693. http://dx.doi.org/10.1034/j.1600-0854.2002.30909.x

Di Pietro, S.M., J.M. Falcón-Pérez, and E.C. Dell'Angelica. 2004. Characterization of BLOC-2, a complex containing the Hermansky-Pudlak syndrome proteins HPS3, HPS5 and HPS6. *Traffic*. 5:276–283. http://dx.doi.org/10.1111/j.1600-0854.2004.0171.x

Di Pietro, S.M., J.M. Falcón-Pérez, D. Tenza, S.R.G. Setty, M.S. Marks, G. Raposo, and E.C. Dell'Angelica. 2006. BLOC-1 interacts with BLOC-2 and the AP-3 complex to facilitate protein trafficking on endosomes. *Mol. Biol. Cell*. 17:4027–4038. http://dx.doi.org/10.1091/mbc.E06-05-0379

Gautam, R., S. Chintala, W. Li, Q. Zhang, J. Tan, E.K. Novak, S.M. Di Pietro, E.C. Dell'Angelica, and R.T. Swank. 2004. The Hermansky-Pudlak syndrome 3 (cocoa) protein is a component of the biogenesis of lysosome-related organelles complex-2 (BLOC-2). *J. Biol. Chem.* 279:12935–12942. http://dx.doi.org/10.1074/jbc.M311311200

Gerondopoulos, A., L. Langemeyer, J.-R. Liang, A. Linford, and F.A. Barr. 2012. BLOC-3 mutated in Hermansky-Pudlak syndrome is a Rab32/38 guanine nucleotide exchange factor. *Curr. Biol.* 22:2135–2139. http://dx.doi.org/10.1016/j.cub.2012.09.020

Helip-Wooley, A., W. Westbroek, H. Dorward, M. Mommaas, R.E. Boissy, W.A. Gahl, and M. Huizing. 2005. Association of the Hermansky-Pudlak syndrome type-3 protein with clathrin. *BMC Cell Biol.* 6:33. http://dx.doi.org/10.1186/1471-2121-6-33

Helip-Wooley, A., W. Westbroek, H.M. Dorward, A. Koshoffer, M. Huizing, R.E. Boissy, and W.A. Gahl. 2007. Improper trafficking of melanocyte-specific proteins in Hermansky-Pudlak syndrome type-5. *J. Invest. Dermatol.* 127:1471–1478. http://dx.doi.org/10.1038/sj.jid.5700737

Huizing, M., R. Sarangarajan, E. Strovel, Y. Zhao, W.A. Gahl, and R.E. Boissy. 2001. AP-3 mediates tyrosinase but not TRP-1 trafficking in human melanocytes. *Mol. Biol. Cell*. 12:2075–2085. http://dx.doi.org/10.1091/mbc.12.7.2075

Huizing, M., A. Helip-Wooley, W. Westbroek, M. Gunay-Aygun, and W.A. Gahl. 2008. Disorders of lysosome-related organelle biogenesis: clinical and molecular genetics. *Annu. Rev. Genomics Hum. Genet.* 9:359–386. http://dx.doi.org/10.1146/annurev.genom.9.081307.164303

Huizing, M., B. Pederson, R.A. Hess, A. Griffin, A. Helip-Wooley, W. Westbroek, H. Dorward, K.J. O'Brien, G. Golas, E. Tsilou, et al. 2009. Clinical and cellular characterisation of Hermansky-Pudlak syndrome type 6. *J. Med. Genet.* 46:803–810. http://dx.doi.org/10.1136/jmg.2008.065961

Jackson, L.P., D. Kümmel, K.M. Reinisch, and D.J. Owen. 2012. Structures and mechanisms of vesicle coat components and multisubunit tethering complexes. *Curr. Opin. Cell Biol.* 24:475–483. http://dx.doi.org/10.1016/j.ceb.2012.05.013

Jaqaman, K., D. Loerke, M. Mettlen, H. Kuwata, S. Grinstein, S.L. Schmid, and G. Danuser. 2008. Robust single-particle tracking in live-cell time-lapse sequences. *Nat. Methods*. 5:695–702. http://dx.doi.org/10.1038/nmeth.1237

Kelly, B.T., A.J. McCoy, K. Späte, S.E. Miller, P.R. Evans, S. Höning, and D.J. Owen. 2008. A structural explanation for the binding of endocytic dileucine motifs by the AP2 complex. *Nature*. 456:976–979. http://dx.doi.org/10.1038/nature07422

Li, K., L. Yang, C. Zhang, Y. Niu, W. Li, and J.J. Liu. 2014. HPS6 interacts with dynactin p150Glued to mediate retrograde trafficking and maturation of lysosomes. *J. Cell Sci.* 127:4574–4588. http://dx.doi.org/10.1242/jcs.141978

Marks, M.S., L. Woodruff, H. Ohno, and J.S. Bonifacino. 1996. Protein targeting by tyrosine- and di-leucine-based signals: evidence for distinct saturable components. *J. Cell Biol.* 135:341–354. http://dx.doi.org/10.1083/jcb.135.2.341

Marks, M.S., H.F.G. Heijnen, and G. Raposo. 2013. Lysosome-related organelles: unusual compartments become mainstream. *Curr. Opin. Cell Biol.* 25:495–505. http://dx.doi.org/10.1016/j.ceb.2013.04.008

Maxfield, F.R., and T.E. McGraw. 2004. Endocytic recycling. *Nat. Rev. Mol. Cell Biol.* 5:121–132. http://dx.doi.org/10.1038/nrm1315

Morita, S., T. Kojima, and T. Kitamura. 2000. Plat-E: an efficient and stable system for transient packaging of retroviruses. *Gene Ther.* 7:1063–1066. http://dx.doi.org/10.1038/sj.gt.3301206

Newton, J.M., O. Cohen-Barak, N. Hagiwara, J.M. Gardner, M.T. Davisson, R.A. King, and M.H. Brilliant. 2001. Mutations in the human orthologue of the mouse underwhite gene (uw) underlie a new form of oculocutaneous albinism, OCA4. *Am. J. Hum. Genet.* 69:981–988. http://dx.doi.org/10.1086/324340

Novak, E.K., S.W. Hui, and R.T. Swank. 1984. Platelet storage pool deficiency in mouse pigment mutations associated with seven distinct genetic loci. *Blood*. 63:536–544.

Novak, E.K., H.O. Sweet, M. Prochazka, M. Parentis, R. Soble, M. Reddington, A. Cairo, and R.T. Swank. 1988. Cocoa: a new mouse model for platelet storage pool deficiency. *Br. J. Haematol.* 69:371–378. http://dx.doi.org/10.1111/j.1365-2141.1988.tb02376.x

Prekeris, R., J. Klumperman, Y.A. Chen, and R.H. Scheller. 1998. Syntaxin 13 mediates cycling of plasma membrane proteins via tubulovesicular recycling endosomes. *J. Cell Biol.* 143:957–971. http://dx.doi.org/10.1083/jcb.143.4.957

Raposo, G., and M.S. Marks. 2007. Melanosomes—dark organelles enlighten endosomal membrane transport. *Nat. Rev. Mol. Cell Biol.* 8:786–797. http://dx.doi.org/10.1038/nrm2258

Raposo, G., M.J. Kleijmeer, G. Posthuma, J.W. Slot, and H.J. Geuze. 1997. Immunogold labeling of ultrathin cryosections: application in immunology. *In* Handbook of Experimental Immunology. Vol. 4. L.A. Herzenberg, D. Weir, L.A. Herzenberg, and C. Blackwell, editors. Blackwell Science, Inc., Cambridge, MA. 1–11.

Raposo, G., D. Tenza, D.M. Murphy, J.F. Berson, and M.S. Marks. 2001. Distinct protein sorting and localization to premelanosomes, melanosomes, and lysosomes in pigmented melanocytic cells. *J. Cell Biol.* 152:809–824. http://dx.doi.org/10.1083/jcb.152.4.809

Raposo, G., M.S. Marks, and D.F. Cutler. 2007. Lysosome-related organelles: driving post-Golgi compartments into specialisation. *Curr. Opin. Cell Biol.* 19:394–401. http://dx.doi.org/10.1016/j.ceb.2007.05.001

Richmond, B., M. Huizing, J. Knapp, A. Koshoffer, Y. Zhao, W.A. Gahl, and R.E. Boissy. 2005. Melanocytes derived from patients with Hermansky-Pudlak Syndrome types 1, 2, and 3 have distinct defects in cargo trafficking. *J. Invest. Dermatol.* 124:420–427. http://dx.doi.org/10.1111/j.0022-202X.2004.23585.x

Salazar, G., B. Craige, M.L. Styers, K.A. Newell-Litwa, M.M. Doucette, B.H. Wainer, J.M. Falcon-Perez, E.C. Dell'Angelica, A.A. Peden, E. Werner, and V. Faundez. 2006. BLOC-1 complex deficiency alters the targeting of adaptor protein complex-3 cargoes. *Mol. Biol. Cell*. 17:4014–4026. http://dx.doi.org/10.1091/mbc.E06-02-0103

Salazar, G., S. Zlatic, B. Craige, A.A. Peden, J. Pohl, and V. Faundez. 2009. Hermansky-Pudlak syndrome protein complexes associate with phosphatidylinositol 4-kinase type II α in neuronal and non-neuronal cells. *J. Biol. Chem.* 284:1790–1802. http://dx.doi.org/10.1074/jbc.M805991200

Sandvig, K., T. Skotland, B. van Deurs, and T.I. Klokk. 2013. Retrograde transport of protein toxins through the Golgi apparatus. *Histochem. Cell Biol.* 140:317–326. http://dx.doi.org/10.1007/s00418-013-1111-z

Setty, S.R.G., D. Tenza, S.T. Truschel, E. Chou, E.V. Sviderskaya, A.C. Theos, M.L. Lamoreux, S.M. Di Pietro, M. Starcevic, D.C. Bennett, et al. 2007. BLOC-1 is required for cargo-specific sorting from vacuolar early endosomes toward lysosome-related organelles. *Mol. Biol. Cell*. 18:768–780. http://dx.doi.org/10.1091/mbc.E06-12-1066

Setty, S.R.G., D. Tenza, E.V. Sviderskaya, D.C. Bennett, G. Raposo, and M.S. Marks. 2008. Cell-specific ATP7A transport sustains copper-dependent tyrosinase activity in melanosomes. *Nature*. 454:1142–1146. http://dx.doi.org/10.1038/nature07163

Sitaram, A., and M.S. Marks. 2012. Mechanisms of protein delivery to melanosomes in pigment cells. *Physiology (Bethesda)*. 27:85–99. http://dx.doi.org/10.1152/physiol.00043.2011

Sitaram, A., R. Piccirillo, I. Palmisano, D.C. Harper, E.C. Dell'Angelica, M.V. Schiaffino, and M.S. Marks. 2009. Localization to mature melanosomes by virtue of cytoplasmic dileucine motifs is required for human OCA2 function. *Mol. Biol. Cell*. 20:1464–1477. http://dx.doi.org/10.1091/mbc.E08-07-0710

Sitaram, A., M.K. Dennis, R. Chaudhuri, W. De Jesus-Rojas, D. Tenza, S.R.G. Setty, C.S. Wood, E.V. Sviderskaya, D.C. Bennett, G. Raposo, et al. 2012. Differential recognition of a dileucine-based sorting signal by AP-1 and AP-3 reveals a requirement for both BLOC-1 and AP-3 in delivery of OCA2 to melanosomes. *Mol. Biol. Cell*. 23:3178–3192. http://dx.doi.org/10.1091/mbc.E11-06-0509

Suzuki, T., W. Li, Q. Zhang, E.K. Novak, E.V. Sviderskaya, A. Wilson, D.C. Bennett, B.A. Roe, R.T. Swank, and R.A. Spritz. 2001. The gene mutated in cocoa mice, carrying a defect of organelle biogenesis, is a homologue of the human Hermansky-Pudlak syndrome-3 gene. *Genomics*. 78:30–37. http://dx.doi.org/10.1006/geno.2001.6644

Sviderskaya, E.V., S.P. Hill, T.J. Evans-Whipp, L. Chin, S.J. Orlow, D.J. Easty, S.C. Cheong, D. Beach, R.A. DePinho, and D.C. Bennett. 2002. p16(Ink4a) in melanocyte senescence and differentiation. *J. Natl. Cancer Inst.* 94:446–454. http://dx.doi.org/10.1093/jnci/94.6.446

Theos, A.C., D. Tenza, J.A. Martina, I. Hurbain, A.A. Peden, E.V. Sviderskaya, A. Stewart, M.S. Robinson, D.C. Bennett, D.F. Cutler, et al. 2005. Functions of adaptor protein (AP)-3 and AP-1 in tyrosinase sorting from endosomes to melanosomes. *Mol. Biol. Cell*. 16:5356–5372. http://dx.doi.org/10.1091/mbc.E05-07-0626

Theos, A.C., J.F. Berson, S.C. Theos, K.E. Herman, D.C. Harper, D. Tenza, E.V. Sviderskaya, M.L. Lamoreux, D.C. Bennett, G. Raposo, and M.S. Marks. 2006. Dual loss of ER export and endocytic signals with altered melanosome morphology in the *silver* mutation of Pmel17. *Mol. Biol. Cell*. 17:3598–3612. http://dx.doi.org/10.1091/mbc.E06-01-0081

Truschel, S.T., S. Simoes, S.R.G. Setty, D.C. Harper, D. Tenza, P.C. Thomas, K.E. Herman, S.D. Sackett, D.C. Cowan, A.C. Theos, et al. 2009. ESCRT-I function is required for Tyrp1 transport from early endosomes to the melanosome limiting membrane. *Traffic*. 10:1318–1336. http://dx.doi.org/10.1111/j.1600-0854.2009.00955.x

Warren, R.A., F.A. Green, and C.A. Enns. 1997. Saturation of the endocytic pathway for the transferrin receptor does not affect the endocytosis of the epidermal growth factor receptor. *J. Biol. Chem.* 272:2116–2121. http://dx.doi.org/10.1074/jbc.272.4.2116

Wasmeier, C., M. Romao, L. Plowright, D.C. Bennett, G. Raposo, and M.C. Seabra. 2006. Rab38 and Rab32 control post-Golgi trafficking of melanogenic enzymes. *J. Cell Biol.* 175:271–281. http://dx.doi.org/10.1083/jcb.200606050

Wei, A.-H., and W. Li. 2013. Hermansky-Pudlak syndrome: pigmentary and non-pigmentary defects and their pathogenesis. *Pigment Cell Melanoma Res*. 26:176–192. http://dx.doi.org/10.1111/pcmr.12051

Zhang, Q., B. Zhao, W. Li, N. Oiso, E.K. Novak, M.E. Rusiniak, R. Gautam, S. Chintala, E.P. O'Brien, Y. Zhang, et al. 2003. Ru2 and Ru encode mouse orthologs of the genes mutated in human Hermansky-Pudlak syndrome types 5 and 6. *Nat. Genet.* 33:145–153. http://dx.doi.org/10.1038/ng1087